A phenology- and trend-based approach for accurate mapping of sea-level

2 driven coastal forest retreat

- 3 Yaping Chen*, Matthew L. Kirwan
- 4 Virginia Institute of Marine Science, College of William and Mary, Gloucester Point, VA, USA
- 5 * Corresponding author
- 6 E-mail addresses: ychen@vims.edu (Y. Chen), kirwan@vims.edu (M. Kirwan).

ABSTRACT

1

7 8

9

10

11

12

13

14

15

16

17

18

19

20

21

22

The rapid replacement of upland forest by encroaching marshland is a striking manifestation of global sea-level rise (SLR). Timely and high-resolution information on the location and extent of transition forest (the ecotone between upland forest and marsh where tree mortality due to seawater intrusion begins) is fundamental to understanding the processes and patterns of SLR-driven landscape reorganization. Despite its significance, accurate characterization of salt-impacted transition forest remains challenging due to the complexity of coastal environments, scarcity of ground-truth data, and the lack of effective mapping algorithms. Here we use the full archive of Landsat images between 1984-2021 to investigate the spectral, temporal, and phenological characteristics of transition forest, and develop a robust framework for monitoring coastal vegetation shifts in the mid-Atlantic U.S., a global SLR hotspot. We found that transition forest exhibits strong negative NDVI trends and a deviation of land surface phenology from marsh and upland forest that distinguishes itself from surrounding vegetation. By integrating temporal trends and land surface phenology, our results demonstrate superior discrimination between marsh and coastal forests to existing map products (e.g. NOAA Coastal Change Analysis Program, National Land Cover Database) that allows a reliable identification of the coastal treeline. We applied the

approach to map regional land cover in 1985, 2000 and 2020 (overall classification accuracy > 92%) and found that the area of coastal forest decreased by 22.0% from 1985 to 2020, the majority of which transitioned to marshland (92.3%, 5.3×10^3 ha). Based upon fine-scale patterns of coastal transgression, we created a practical workflow for spatially explicit quantification of forest retreat rates. Concurrent with rising sea level, coastal forests migrated upslope from 0.63 ± 0.27 m above sea level in 1985 to 0.78 ± 0.32 m above sea level in 2020, and horizontal forest retreat rates accelerated from 3.1 (range of 0-36) m yr⁻¹ during 1985-2000 to 4.7 ± 0.25) m yr⁻¹ during 2001-2020. As SLR continues to accelerate, our study may serve as a scalable solution for consistent tracking of coastal landscape evolution that is urgently needed for sustainable forest and wetland management.

Keywords: sea-level rise, saltwater intrusion, forest degradation, marsh encroachment, coastal
 treeline

1. INTRODUCTION

Widespread vegetation shifts as a response to anthropogenic climate change have attracted global attention over recent decades (Chen et al., 2021a; Kirwan and Gedan, 2019; Kirwan and Megonigal, 2013; Osland et al., 2022). In coastal environments, climate-driven sea-level rise (SLR) has triggered massive landward marsh migration and forest retreat (Kirwan and Gedan, 2019; Smith and Kirwan, 2021), with potentially large negative impacts to the delivery of essential ecosystem services (e.g. carbon sequestration, disturbance attenuation, and biodiversity conservation) to human populations (Gedan et al., 2011; Smart et al., 2020; Smith and Kirwan, 2021). A refined understanding of when, where and how coastal transgression proceeds with rising

sea level is imperative to allow informed decisions for sustainable coastal development. However, current knowledge on the spatiotemporal patterns of coastal vegetation shift remains fragmented, partly constrained by the scarcity of long-term, ground-based information and the lack of effective mapping algorithms across spectrally complex coastal settings.

As compared to other types of land cover/use change (e.g. forest to cropland or urban area), the conversion of upland forest to marsh induced by rising sea level is usually a gradual, subtle process without clear-cut boundaries (Kirwan and Gedan, 2019; Ury et al., 2021). Progressive salt intrusion in low-relief coastal terrains normally leads to the prevalence of transition forests (i.e. "ghost forests") that define the ecotone between marsh and upland forest, and are characterized by a complex mixture of live and standing-dead trees with an emerging understory of intruding marsh and shrubs (Smith and Kirwan, 2021; Walters et al., 2021). The presence of this transition zone poses great challenges for coherent, automatic tracking of the coastal treeline. As a result, previous studies on SLR-driven coastal forest retreat rely heavily on visual interpretation of local, ultra high-resolution aerial imagery to delineate the marsh-forest boundary (Flester and Blum, 2020; Schieder and Kirwan, 2019; Smith, 2013). Aside from being labor-intensive and time-consuming, this approach precludes consistent application over large spatial scales.

Regional studies on the distribution and trajectory of coastal forest or marsh typically rely on standardized remote-sensing products (Byrd et al., 2018; He et al., 2022; White et al., 2021). In the US, it commonly refers to the NOAA Coastal Change Analysis Program (C-CAP) dataset (i.e. the coastal expression of the National Land Cover Database, NLCD) (NOAA Office for Coastal Management, 2016). The C-CAP dataset takes advantage of the native 30 m resolution Landsat images acquired from contrasting seasons in conjunction with ancillary data to map 25 categories

of coastal land cover for conterminous US every 4-6 years. In spite of its overall success at capturing broad-scale patterns, the C-CAP dataset is not specifically designed to distinguish between marsh and forest, and it does not map salt-stressed transition forest. In fact, previous research comparing the C-CAP dataset with field observations reveals appreciable classification error at the marsh-forest interface (Weis et al., 2020). Similarly, studies using Landsat images acquired in summer and winter to quantify the extent of forest retreat in coastal North Carolina also show frequent confusion between migrating forest and surrounding marsh (Smart et al., 2020; Ury et al., 2021). Accordingly, a more advanced mapping algorithm explicitly targeted at the intricate transition forest is required to allow reliable monitoring of coastal forest at regional to global scales.

Recent studies incorporating land surface phenology derived from the entire annual Landsat time-series suggest enhanced classification accuracy than those based solely upon multi-seasonal images in various spectrally challenging environments (Diao and Wang, 2016; Thomas et al., 2021). For instance, by integrating a range of phenological metrics extracted from monthly Landsat dataset, studies in a riparian ecosystem successfully differentiated exotic saltcedar from native vegetation (Diao and Wang, 2018, 2016). In a fast-changing coastal wetland, the phenological-based approach allowed nuanced depiction of *Spartina alterniflora* invasion over past decades (Tian et al., 2020). Similarly, in a mountainous region of the eastern U.S., a study leveraged the phenological deviation of thinning forest from intact forest to pinpoint areas of active management (Thomas et al., 2021). Despite success in previous application, whether land surface phenology can be exploited to map transition forest remains unknown. Literature and field survey suggest that seawater intrusion may indeed provoke a departure of land surface phenology in transition

forest, as reflected by muted seasonality (White and Kaplan, 2021), delayed budding, and early onset of leaf senescence (Chen and Ye, 2013; Y. Chen and Ye, 2014; Munns and Tester, 2008) – all of which may be detected by remote-sensing platforms. It is thereby desirable to explore the phenological features unique to transition forest for improved separability of coastal forest from marsh.

In addition, previous studies suggest that ecosystems subjected to chronic stressor or regime shifts usually undergo predictable directional changes in structure and function, such as change of biomass and productivity (Berner et al., 2018; Smith and Kirwan, 2021), shift in tree age distribution and plant composition (Bégin, 1990; Clark, 1986), and amplification of ecosystem variance (Scheffer et al., 2015). Built upon expected temporal trajectory of forest biomass, a study was able to identify hotspots of seawater intrusion in eight coastal wetlands using MODIS timeseries between 2000 and 2018 (White and Kaplan, 2021). In similar fashion, recent studies in high-latitudes associate multi-decadal Landsat-based NDVI trends with areas of active tundra shrubification, where native graminoid tundra is replaced by productive intruding shrubs (Berner et al., 2018; Chen et al., 2021a). Hence, promise may be held by temporal trend analyses of satellite-derived vegetation indices (e.g. NDVI, a proxy of biomass and productivity) to discriminate the ecologically-unique transition forest from the spectrally-similar surroundings.

Given current information, the objectives of our study are (1) to develop a phenology- and trend-based algorithm focusing on the transition forest as a means to optimize the separation of coastal forest from marsh; and (2) to apply the algorithm and accurately map coastal vegetation in 1985, 2000 and 2020 to quantify the spatiotemporal patterns of coastal transgression. As the ecological and socioeconomic impacts of SLR accelerate (Bhattachan et al., 2018; Kulp and

Strauss, 2019), our quantitative and scalable approach to characterize sea-level driven landscape reorganization may prompt new scientific understanding of complex ecological processes, and management actions that better prepare coastal ecosystems and societies for future climate change.

2. MATERIALS AND METHODS

2.1 Study region

110

111

112

113

114

115

116

117

118

119

120

121

122

123

124

125

126

127

128

129

130

131

Our study area (1,009 km²) is located in the rapidly-changing Chesapeake Bay region of the U.S. mid-Atlantic coast (38.5° N, 76.3° W), and encompasses the iconic Blackwater National Wildlife Refuge (Fig. 1). As a pilot study, we intentionally selected this region as our study area for three reasons. First, it is among coastal ecosystems most threatened by global SLR (Fig. 2), where the SLR rate is 2 to 3 times faster than global average (Sallenger et al., 2012). Second, rapid SLR has led to expansive formation of "ghost forest" in the region spanning a gradient of coastal topography (Kirwan and Gedan, 2019; Schieder et al., 2018), which allows us to test the performance of our algorithms across complex environmental context (Fig. 3). Third, the study region is relatively rural with minimal human intervention, which serves as a natural canvas for coastal transgression to occur (Fig. 1). More than 85% of the region falls within a narrow elevation range between 0 and 3 m NAVD (North American Vertical Datum of 1988, which approximates regional mean sea level), making the ecosystem extremely vulnerable to additional SLR. We studied all areas between 0 and 5 m NAVD in the region, an elevation range that encompasses permanently flooded bays and ponds, through intertidal wetlands, to adjacent uplands that have no sign of tidal inundation. Farmland and urban development (e.g. impervious surface) combined only account for ~10% of the land surface in the study region, mostly in high elevations. Hence, the regional landscape primarily

consists of a natural mosaic of marshes, transition forests and upland forests, interspersed with a network of ponds and channels (Fig. 1). All elevation data refers to the high precision Coastal National Elevation Database (CoNED DEM) (Danielson et al., 2018).



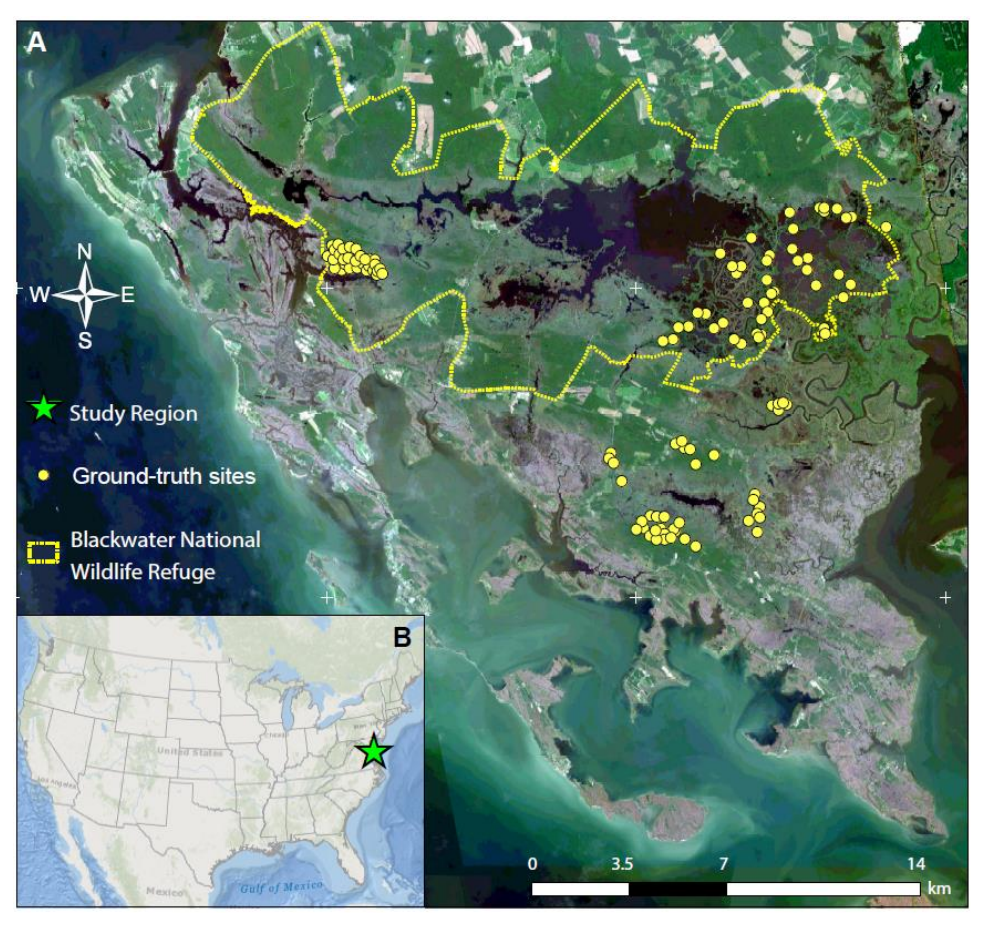


Fig. 1. Map showing the study region (A) which is located on the U.S. mid-Atlantic coast (B). The study region represents the mid-Atlantic sea-level rise hotspot and it encompasses the ecologically and culturally important Blackwater National Wildlife Refuge outlined in yellow. The yellow dots indicate our ground-truth sites in the study region. In addition to ground-truth data, the reference sites for our land cover classification also include sites selected from contemporary drone images and high-resolution aerial photos.

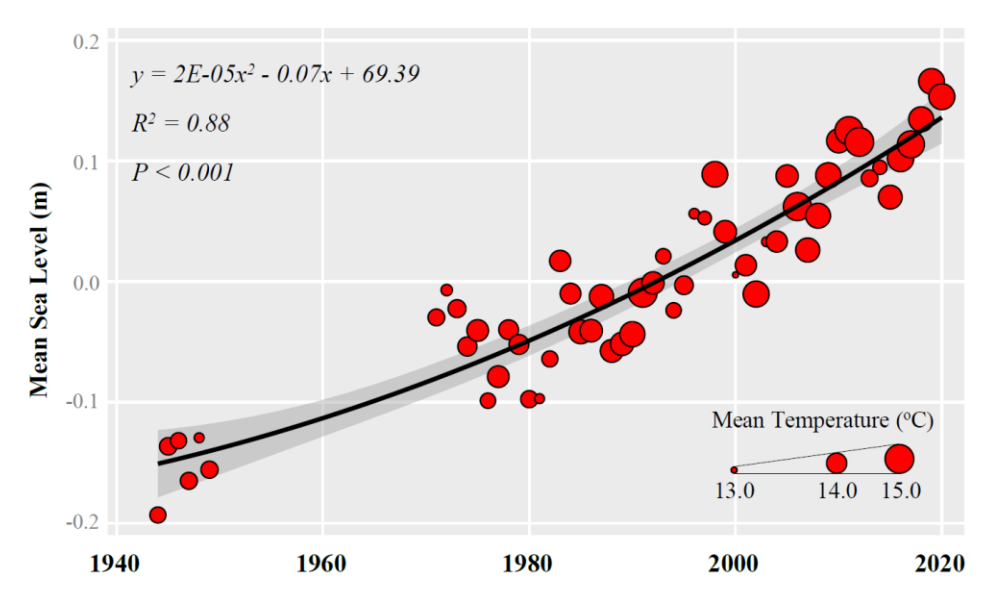


Fig. 2. Accelerated sea-level rise and warming climate in the study region. The data plotted here refers to the long-term temperature and tidal observations at the nearest NOAA meteorological station in Dover, Delaware and the nearest NOAA Tides and Currents station in Cambridge, Maryland.

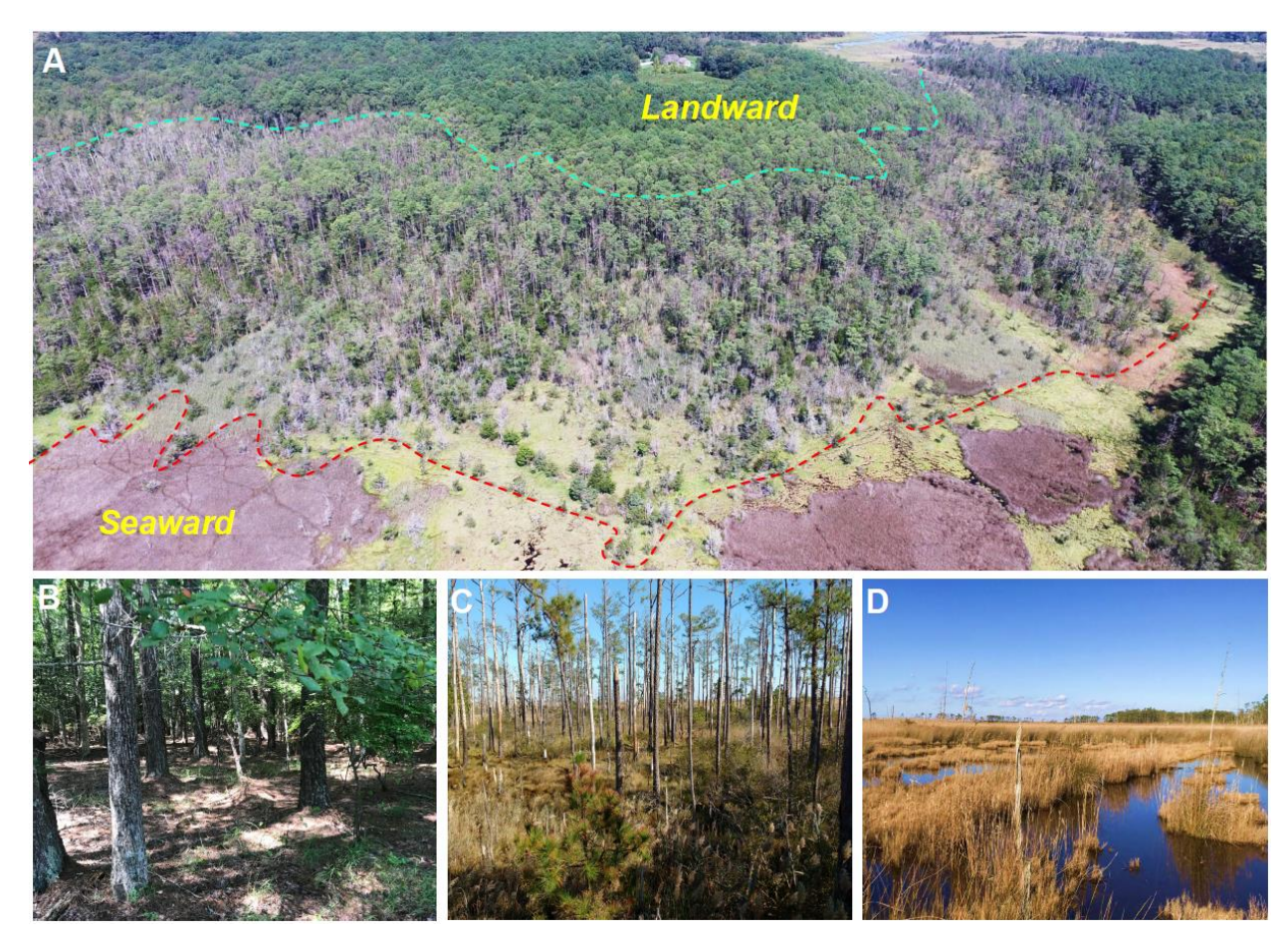


Fig. 3. Coastal landscape reorganization with rising sea-level. (A) Broad-scale vegetation distribution along the land-sea margin, highlighting a "ghost forest" transition zone with dead and stressed trees. (B) Landward upland forest with a closed canopy and lack of understory vegetation. (C) Transition forest undergoing active seawater intrusion, where forest die-off leads to increased light availability for shrub growth and marsh transgression. (D) Established marshland with occasional remnant standing-dead trees, signifying the completion of marsh transgression.

2.2 Image acquisition and preprocessing

We gathered all orthorectified, Tier-1 Landsat surface reflectance scenes covering the study region between 1984 and 2021 with cloud cover less than 60% (n = 3,130) from the USGS EarthExplorer (https://earthexplorer.usgs.gov/) collected by Landsat-5 TM, Landsat-7 ETM+ and Landsat-8 OLI. All Landsat images were delivered in a geometrically and radiometrically corrected fashion, and

each contains six spectral bands: the three visible bands (blue, green and red), the Near-Infrared band (NIR), and the two Shortwave-Infrared bands (SWIR1 and SWIR2). All images were processed using the ancillary Quality Assessment datasets to mask pixels associated with missing data, cloud, cloud shadow, and snow and ice (Ihlen and Zanter, 2019a, 2019b; Zhu et al., 2015). The multispectral NDVI index, a commonly used vegetation index, was employed in this study as a proxy of vegetation phenology (Thomas et al., 2021; Zhang et al., 2022) and ecosystem biomass and productivity (Berner et al., 2018; Chen et al., 2020; Zoffoli et al., 2020). We computed the NDVI index associated with each image using the red and NIR bands processed above. Residual cloud, haze and shadows were further filtered by thresholding the blue (surface reflectance > 0.07) and red (surface reflectance < 0.01) bands (Ju and Masek, 2016). Since the dataset spans multiple generations of Landsat sensors that slightly differ in spectral range of individual bands, cross-sensor correction of NDVI was performed to ensure temporal consistency (Berner et al., 2020; Roy et al., 2016). Additionally, intertidal ecosystems are periodically flooded with tidal water that may compromise the performance of vegetation indices for trend detection (O'Connell et al., 2017). To constrain tidal influence, we applied the Tidal Marsh Inundation Index on each image to remove pixels of partial inundation before further analysis (Campbell and Wang, 2020; O'Connell et al., 2017). The resulting products were used to generate two data stacks: one for analyzing recurrent vegetation phenological patterns that contains the entre time-series of NDVI images within a year stacked annually by Day of Year (DOY) during 1984-2021; and the other for decadal trend analysis, containing only peak growing-season (July-August) NDVI dataset stacked in time series from 1984 to 2021.

2.3 Field campaign and coastal vegetation inventory

161

162

163

164

165

166

167

168

169

170

171

172

173

174

175

176

177

178

179

180

181

In the summer of 2020 and 2021, we undertook several field campaigns to collect ground-truth data of different coastal vegetation types across the study region (Fig. 1). We recorded the location and vegetation type at each ground-truthing site throughout the region with a minimum betweensite distance of 150 m. We also inventoried coastal vegetation and acquired drone images across transects spanning the upland-marsh gradient at Moneystump Swamp within the Blackwater National Wildlife Refuge (Fig. 1). According to our field survey, here we define upland forest as the coastal forest free from seawater intrusion, as reflected by a closed forest canopy, sparse understory vegetation due to limited light availability, and absolute absence of marsh vegetation on the forest floor (Fig. 3B, Table 1). As expected, transition forests usually proliferate in lowlying terrains at the interface between upland forest and marsh (Fig. 3A). Transition forest is characterized by a mixture of live and dead trees with intruding marsh present in forest understory (Fig. 3C, Table 1). The transition forest is highly heterogenous across the study region (Fig. 1), reflecting various stages of coastal forest retreat associated with rising sea level (Smith and Kirwan, 2021). To ensure that our ground truth data represent the full spectrum of transitioning forests, we selected the sites along the entire marsh-forest ecotone at Moneystump Swamp that incorporated canopy cover estimates in transition forest ranging from 10% (adjacent to marsh) to 75% (adjacent to upland forest). Marsh is the most expansive coastal vegetation in the study region, showing nearly continuous distribution extending from the forest margin until far towards the sea. We collected ground truth data for different marsh types that distribute following broad biophysical gradients in the study region (Fig. 1). Specifically, here we define marsh as the intertidal habitat consisting entirely of marsh species, although fragments of dead trees are

183

184

185

186

187

188

189

190

191

192

193

194

195

196

197

198

199

200

201

202

occasionally spotted in newly formed marshlands (Fig. 3D) - a lasting indicator of rapid forest loss with the rising sea.

Table 1: Definition of the land cover types mapped in this study.

Land cover	Definition
Marsh	Tidal wetlands dominated by herbaceous hydrophytes like cordgrass, rushes, and sedges.
Transition forest	Low-lying forests between marsh and upland forests where mortality due to seawater intrusion has already begun. Also known as ghost forests, with marshes and/or shrubs present in understory.
Upland forest	Primary or long-standing secondary forests characterized by closed canopy and mature trees of height greater than 5 m.
Water	Open water with 20% or less of vegetation and soil cover.
0.1 *	Other (Agriculture): agricultural lands, including actively cultivated, fallow or recently abandoned croplands, and pasture and residential lawns.
Other*	Other (Urban area): impervious surface, such as roads and concrete constructions for residential or commercial activities.

^{*} Other (Agriculture) and Other (Urban area) were classified as separate classes, and the results were grouped to present as a single land cover type (Other) for simplicity.

2.4 Vegetation phenology and phenological metrics

To represent land surface phenology in complex environments, we complemented the ground-truth data with an additional set of reference sites randomly selected ("Create Random Points" in ArcGIS v10.7) from the contemporary drone images and the latest submeter resolution National Agriculture Imagery Program (NAIP) aerial photos across the study region (between-site distance ≥ 150 m). Each of the coastal vegetation types (i.e. upland forest, transition forest, and marsh) has a minimum of 600 reference sites. We assessed vegetation-specific phenological patterns (Fig. 4) in 2020 at the reference sites using a 3-yr NDVI composite following the approach of Thomas et al. (2021). The 3-yr image stack (the previous year, the year of interest, and the following year) was adopted to account for prominent cloud cover of coastal ecosystems and the extended revisit

period of Landsat satellites. All NDVI images were stacked in DOY to yield sufficient monthly data points for modeling annual phenological rhythm (Thomas et al., 2021).

221

222

223

224

225

226

227

228

229

230

231

232

233

234

235

236

237

238

239

240

241

242

analyses were performed in R (v3.6.1).

We first filtered the NDVI time-series (Fig. 4) with five candidate models: the asymmetric Gaussian model (White et al., 1997), the adaptive Savitzky-Golay function, the double-logistic filter (Atkinson et al., 2012; Jönsson and Eklundh, 2004), the Fourier analysis (Brooks et al., 2012), and the Whittaker filter (Eilers, 2003). The models were selected for their efficacy in smoothing time-series data and their robustness in reproducing the land surface phenological profile derived from remotely-sensed NDVI dataset (Atkinson et al., 2012; Diao and Wang, 2016; Thomas et al., 2021). We computed the root mean square error (RMSE) and the coefficient of determination (R^2) to evaluate model performance, and identified the double-logistic filter as the most suitable for our study in simulating land surface phenology with consistent performance across vegetation types. We extracted seven ecologically-significant phenological metrics from the smoothed doublelogistic curves in R (v3.6.1, the 'phenofit' package, (Kong, 2020)) for all reference sites. The set of phenological metrics records important events and patterns of plant growth cycle (Atkinson et al., 2012; Kong et al., 2019), referring to the Start of Growing Season, End of Growing Season, Peak of Growing Season, Length of Growing Season, Base NDVI, Peak NDVI and Annual Amplitude of NDVI. We compared each of the phenological metrics between vegetation types using one-way analysis of variance (ANOVA). All datasets were examined with the Shapiro-Wilk test for normality prior to statistical analysis. Data transformation was conducted to fulfill model assumptions, and difference is considered significant at the level of P < 0.05. All statistical

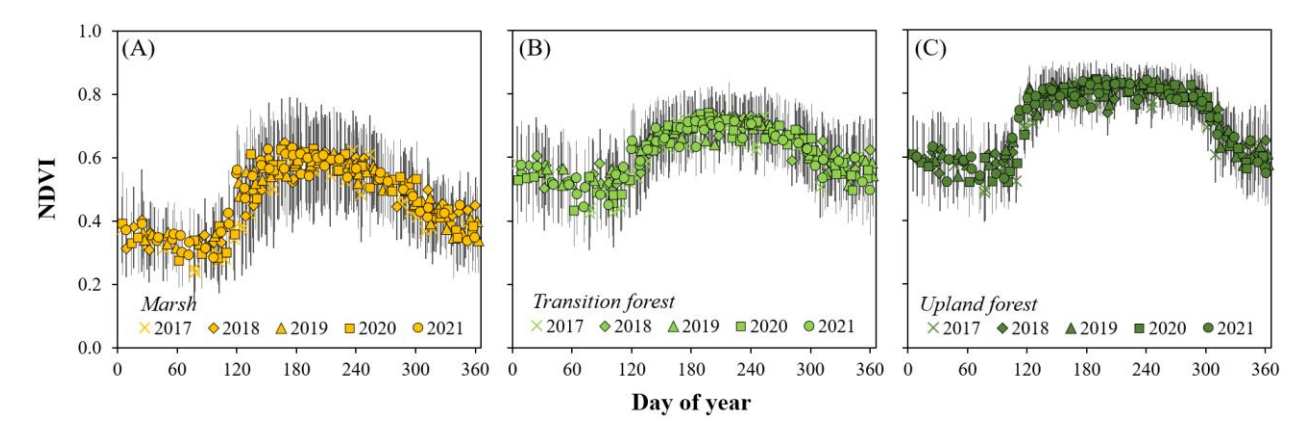


Fig. 4. Annual phenological patterns of marsh (A), transition forest (B), and upland forest (C) estimated with Landsat-based NDVI time-series. Plots show data for the most recent five years, and all results are presented as mean \pm SD.

2.5 Temporal-trend analysis for coastal vegetation

Using the same reference sites collected above for various coastal vegetation types, we conducted another experiment to test whether trend analyses of NDVI time-series can lend additional strength to isolating the ecologically-unique transition forest from adjacent vegetation (Fig. 5). In particular, to explore how temporal length may influence the discriminatory power of trend analysis and whether an optimal time-span exists for trend detection, we performed three trend analyses with varying time-spans (Fig. 5). The first analysis leverages the full length of Landsat time-series between 1984 and 2020 (36 years, the long time-span test), the second test stretches an intermediate time-span from 1996 to 2020 (24 years, the intermediate time-span test), and the third test spans the latest 12 years between 2008 and 2020 (the short time-span test) (Fig. 5).

For each test, we analyzed peak-growing season NDVI time-series for a monotonic temporal-trend (Fig. 5) on each reference site using the rank-based Mann-Kendall trend test (Wang et al., 2020). The slope of the NDVI trend was computed using the non-parametric Theil–Sen slope

estimator (Theil, 1950). All analyses were conducted in R (v3.6.1) with the 'zyp' package (Bronaugh and Werner, 2019). The statistical metrics (R^2_{adj} , P-value, and slope) of different timespan tests were compared between vegetation types to evaluate the performance of the tests in differentiating between coastal vegetation (Fig. 5). For improved confidence in the best time-span scenario, we also formulated a simplistic decision tree model according to vegetation-specific NDVI trend (slope, $Slope_{NDVI\ trend}$; significance, $P_{NDVI\ trend}$) and the NDVI value by the end of the trend analysis ($NDVI_{end}$) (Fig. 5) as below:

269 Transition forest =
$$\begin{cases} 1 \ (Slope_{NDVI\ trend} < 0; P_{NDVI\ trend} < 0.1; \ NDVI_{end} \ge 0.64) \\ 0 \ (Other\ vegetation) \end{cases}$$
 (1)

Using this empirical model, we assessed the efficacy of each time-span test in differentiating between transition forest and others on all reference sites. The best time-span scenario was identified as the one generating maximal separation between coastal vegetation, and it was then used for regional trend analysis in our land cover mapping.

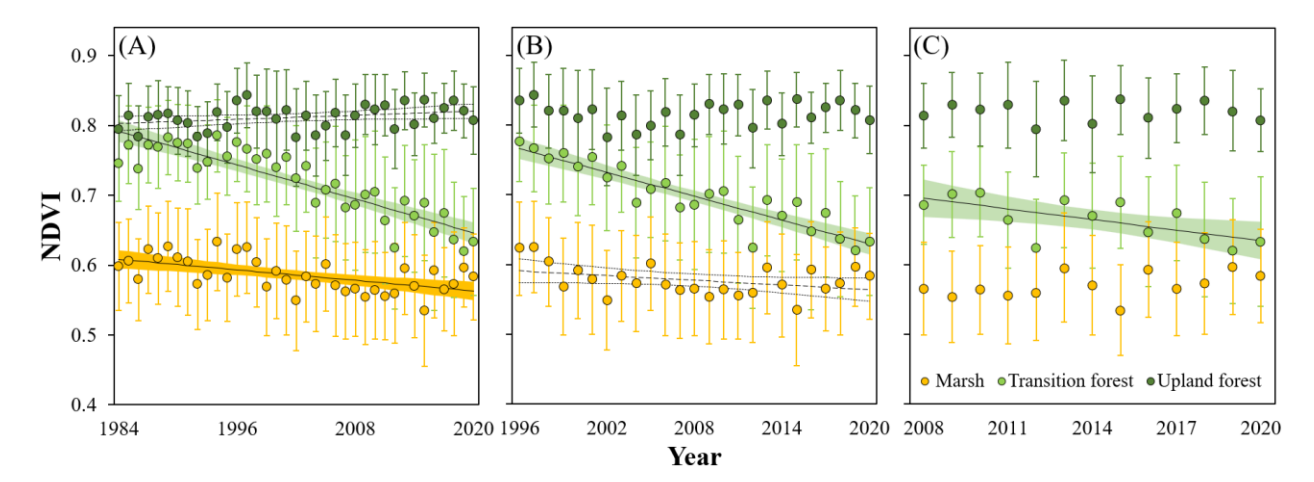


Fig. 5. Temporal-trend of peak growing-season NDVI for different coastal vegetation types, estimated using 36 years of data (1984-2020) – the long time-span test (A), 24 years of data (1996-2020) – the intermediate time-span test (B), and 12 years of data (2008-2020) – the short time-span test (C). The linear regression trend line is bounded by the 95% confidence interval. Dotted lines refer to marginally significant trends ($0.05 \le P < 0.1$) whereas solid lines represent significant trends at the level of P < 0.05.

2.6 Land cover classification and comparison between scenarios

To investigate whether land surface phenology and temporal-trend information can be capitalized on to improve coastal forest mapping, we mapped regional land cover in 2020 with four competing scenarios by incorporating and not incorporating phenological or temporal-trend metrics as model input. The land cover mapped refers to upland forest, transition forest, marsh, open water and other (i.e. agriculture and urban area) (Table 1).

The first scenario (S₁) follows a traditional classification algorithm for coastal forest mapping, using clear sky Landsat images obtained during low tides from contrasting seasons, one in spring-summer (the greening, warm season) and the other during fall-winter (the browning, cold season) (Homer et al., 2015; Smart et al., 2020; Ury et al., 2021). To be consistent, we acquired the two images for S₁ following our annual phenological patterns assessed above (Fig. 4): one in July-

August (warm season) and the other in January-February (cold season) – the timing when intervegetation contrast is maximized. On top of the original Landsat spectral bands, the inputs of S₁ also include thirteen ancillary layers found desirable in previous studies (Belgiu and Csillik, 2018; Gong et al., 2019; Zhang and Yang, 2020), referring to nine multispectral indices computed from Landsat bands and four biophysical metrics derived from the CoNED DEM (Table 2).

The input of the second scenario (S₂) is identical to that of S₁ except that it incorporates an additional set of phenological metrics described in Section 2.4. Similarly, the input of the third scenario (S₃) includes the full set of the S₁ inputs and the statistical metrics derived from temporal-trend analysis using the best time-span scenario identified in Section 2.5. As a comparison, the fourth map (S₄) was generated using all the information above as input, which comprises the S₁ input plus all phenological metrics of S₂ and all statistical metrics of S₃.

We selected the random forest (RF) classifier (Breiman, 2001) implemented in R (v3.6.1, the 'caret' and 'randomForest' packages (Kuhn et al., 2021; Liaw and Wiener, 2002)) to create all land cover maps. As compared to conventional classification algorithms (e.g. Decision Tree, Maximum Likelihood Classifier, and Support Vector Machines), the RF classifier possesses several advantages that make it well suited for our study. Aside from being computationally efficient and sophisticated at handling high dimensionality of input data, the RF demonstrates high classification accuracy across a wide range of terrestrial and wetland ecosystems (Belgiu and Csillik, 2018; Belgiu and Drăgu, 2016; Diao and Wang, 2016; Gong et al., 2019). Recent products generated by RF using land surface phenology have proven successful in differentiating spectrally-similar land cover types (Diao and Wang, 2018, 2016; Thomas et al., 2021). Furthermore, the RF classifier is relatively robust to training errors (up to 20% misinterpretation of training sample,

(Gong et al., 2019)) – an important asset for mapping landscapes undergoing rapid reorganization but lacking timely reference.

All the classification algorithms (S_1 - S_4) were trained and validated with the same reference data. As mentioned earlier, we selected ~600 reference sites for each land cover throughout the study region based on field campaign, drone images, and the NAIP aerial photos. The dataset was randomly divided in the ratio of 50% to 50% for each land cover as training and validation. We set the number of decision trees to 500 for unbiased estimate of generalization error, and used the default number of variables to be tested for split (i.e. square root of the number of input features) for all scenarios (Belgiu and Drăgu, 2016). The classification results were evaluated by confusion matrices and the associated four measures of accuracy (Kappa coefficient, overall accuracy, and *Producer's* and *User's* accuracy). To statistically determine whether incorporating phenological and/or temporal-trend information improves land cover mapping, we compared the results between scenarios using the McNemar's chi-squared test (Belgiu and Csillik, 2018; Diao and Wang, 2016) at the significance level of P < 0.05.

Table 2. Selected inputs for the S₁ classification. The Landsat images were obtained from contrasting seasons of summer (July-August) and winter (January-February) when inter-vegetation contrast is maximized in 2020. All images were acquired during low tide in clear sky.

Categories	Predictors*	Formula/Description	References
Spectral Bands	BLUE GREEN RED NIR SWIR1 SWIR2	Surface reflectance of the blue band Surface reflectance of the green band Surface reflectance of the red band Surface reflectance of the NIR band Surface reflectance of the SWIR band1 Surface reflectance of the SWIR band2	(Diao and Wang, 2018, 2016; Gong et al., 2019; Tian et al., 2020)
Multispectral Indices	NDVI EVI SAVI MSAVI NDWI mNDWI TCP-brightness TCP-greenness TCP-wetness	$NDVI = \frac{NIR-RED}{NIR+RED}$ $EVI = \frac{2.5*(NIR-RED)}{NIR+6*RED-7.5*8LUE+1}$ $SAVI = \frac{1.5*(NIR-RED)}{NIR+RED+0.5}$ $MSAVI = 0.5*(2*NIR+1-\sqrt{(2*NIR+1)^2-8*(NIR-RED)})$ $NDWI = \frac{NIR-SWIR1}{NIR+SWIR1}$ $mNDWI = \frac{Green-SWIR1}{Green+SWIR1}$ Tasseled Cap Transformation computed from surface reflectance of all six spectral bands. Coefficients differ between Landsat TM, Landsat ETM+ and Landsat OLI.	(Belgiu and Csillik, 2018; Belgiu and Drăgu, 2016; Byrd et al., 2018; Smart et al., 2020; Thomas et al., 2021; Zhang and Yang, 2020)
Ancillary data	Elevation Slope Aspect TPI	Computed from the 1 m resolution Coastal National Elevation Database (CoNED) DEM, and resampled to 30 m resolution using bilinear interpolation.	(Belgiu and Drăgu, 2016; Homer et al., 2015)

* NIR: Near-Infrared; SWIR: Shor-wave Infrared; NDVI: Normalized Difference Vegetation Index; EVI: Enhanced Vegetation Index; SAVI: Soil-Adjusted Vegetation Index; MSAVI: Modified SAVI; NDWI: Normalized Difference Water Index; mNDWI: modified NDWI; TCP: Tasseled Cap transformation; TPI: Topographic Position Index.

2.7 Historical mapping and comparison with existing products

Using the classification algorithm identified as the most suitable in Section 2.6, we then created two historical land cover maps (in 1985 and 2000) for the study region following the same procedure as that of 2020 described above. All high-resolution (< 2 m) images used for historical reference were acquired within ± 2 years of the intended year of mapping, referring to the blackwhite or color-infrared aerial photography of NAIP, and the National High-Altitude Photography. We computed the mean elevation of all pixels from the same vegetation type according to the

CoNED DEM at each mapping step (1985, 2000, and 2020) to explore whether the distribution of coastal vegetation shifts towards higher elevations with SLR over time.

We compared our multi-period maps (1985-2000-2020) with other widely-used time-series products, namely the NOAA C-CAP maps and the NLCD database to evaluate coastal forest cover change over past decades. To minimize temporal mismatch between existing products and ours, we acquired the C-CAP maps in 2001 and 2016, as a counterpart to our maps in 2000 and 2020. Similarly, the earliest (in 2001) and the latest (2019) NLCD maps were obtained to ensure maximal comparability with our time of interest.

Next, we computed the differenced maps for all time-series products to quantify net change of coastal forest over the past two decades (the C-CAP maps between 2001-2016; the NLCD maps between 2001-2019; our own maps between 2000-2020). To allow cross-product comparison of coastal forest, we reclassified forest area in the C-CAP/NLCD products, and in our own maps. Specifically, all pixels labeled as deciduous forest, evergreen forest, mixed forest, scrub/shrub, forested wetland and scrub/shrub wetland in the C-CAP maps were reclassified as forest. Similarly, all areas classified as deciduous forest, evergreen forest, mixed forest, scrub/shrub, and woody wetland in the NLCD products were reclassified as forest. In our own maps, forest refers to all areas mapped as upland forest and transition forest. Similarly, the land cover of marsh termed in our maps corresponds to areas represented by palustrine and estuarine emergent wetland in the C-CAP products, and by emergent herbaceous wetlands in the NLCD maps.

2.8 Spatially explicit quantification of forest retreat rate

We analyzed our time-series land cover maps to shed light on the spatiotemporal patterns of SLRdriven coastal forest retreat. Specifically, we created three spatially explicit forest retreat maps (from 1985 to 2000, from 2000 to 2020, and from 1985 to 2020) to explore whether and to what extent forest retreat rate has changed over time. Below we describe our step by step workflow for quantifying forest retreat rate during any two time periods in more detail.

First, we computed the differenced map between Time 1 (T₁) and Time 2 (T₂) to identify areas of forest loss. The map was then converted to smoothed vector features where areas of forest loss were represented by discrete polygons ('Smooth Polygon' tools in ArcGIS v10.7). We studied unique patterns of forest loss, and assigned each of the polygons into one of the four patterns it represents (Fig. 6): Interior Loss (IL: forest interior replaced by emerging marsh, in which area of forest loss is outlined in T₂), Entire Loss (EL: complete conversion of forest to marsh, in which area of forest loss is outlined in T₁), Linear Retreat (LR: parallel forest retreat with the area lost outlined by open forest boundaries in T₁ and T₂), and Radial Retreat (RR: concentric forest retreat, where area of forest loss is delineated by closed boundaries in T₁ and T₂).

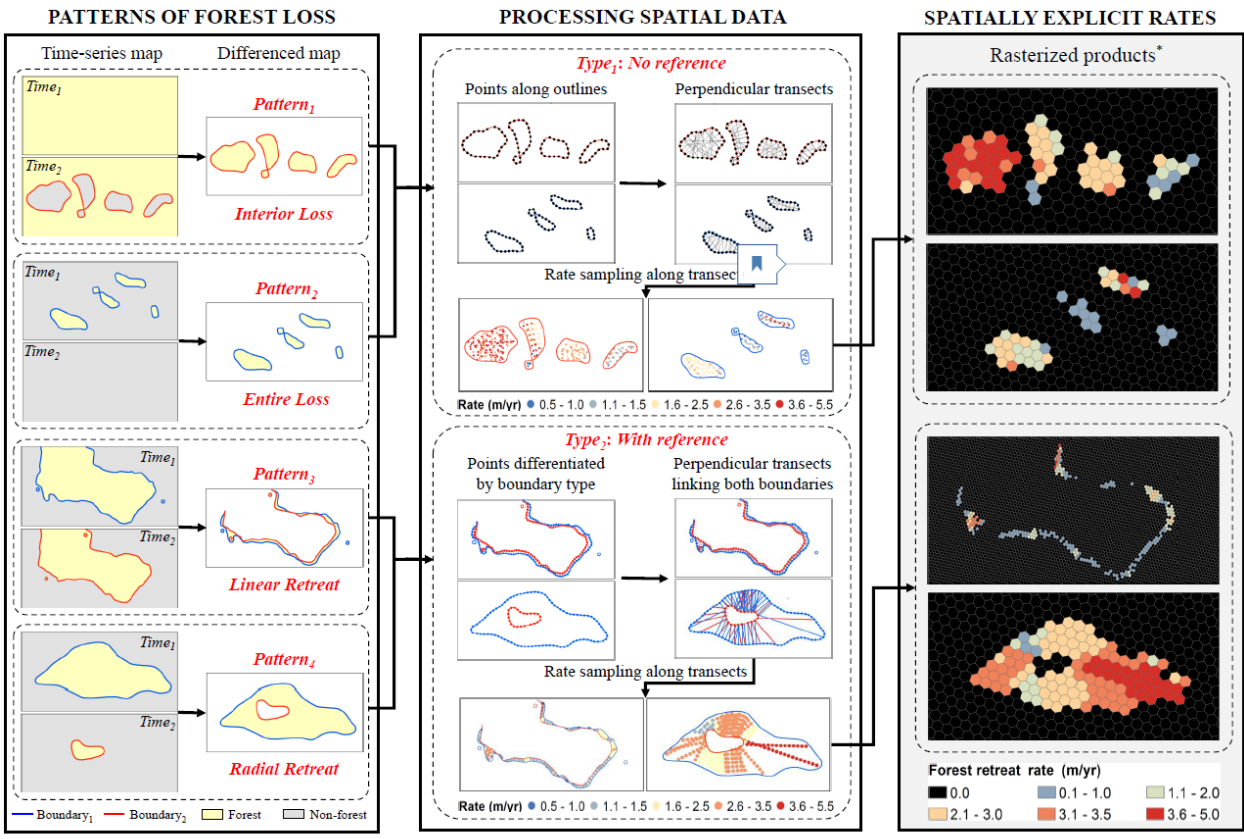
Second, we divided the four patterns of polygons (i.e. areas of forest loss) into two groups (Type₁ and Type₂) depending on the configuration of its boundary (Fig. 6). The Type₁ polygons represent forest loss with no pre-defined baseline (no reference) for specific direction of forest loss, including all IL and EL polygons (Fig. 6), whereas the Type₂ polygons consist of all LR and RR polygons, referring to forest loss with clearly defined baseline (with reference) to indicate directional forest change from T₁ to T₂ (Fig. 6).

Third, we quantified forest retreat rate, separately, for the two types of polygons. To compute forest retreat rate within the Type₁ polygons, we created points along all polygon boundaries ('Generate Points Along Line', ArcGIS v10.7) at regular distances (30 m, one Landsat pixel). Then, we created perpendicular lines at each point ('Create Perpendicular Lines', ArcGIS v10.7) that cut

through the polygon in all directions (Fig. 6). These perpendicular lines stand for potential paths of forest retreat from T_1 to T_2 , and their length thereby represents distance of forest retreat. We divided the length of the perpendicular lines by the number of years between T_1 and T_2 to estimate the rate of forest retreat along each path (Fig. 6).

Next, we computed forest retreat rates within areas represented by the Type₂ polygons. The procedure is identical to that of Type₁ polygons except that the perpendicular lines have to intersect with both the T₁ and T₂ boundaries to represent the directed path of forest retreat (Fig. 6). Instead of placing points along all polygon boundaries as we did for Type₁ polygons, we generated points only on the T₁ boundary of the Type₂ polygon, from where the perpendicular lines extend to intersect with the T₂ boundary ('Create Perpendicular Lines', ArcGIS v10.7). In the same way, we generated points on the T₂ boundary to draw perpendicular lines intersecting the T₁ boundary (Fig. 6). The rate of forest retreat represented by each perpendicular line was calculated in the same way as described above for the Type₁ polygons.

Finally, we sampled forest retreat rates across all areas of forest loss represented by the Type1 and Type2 polygons, and the results were rasterized to produce the spatially-explicit map of forest retreat rate ('Generate Tessellation', ArcGIS v10.7) (Fig. 6). In brief, we sampled points along all perpendicular lines every 30 m (one Landsat pixel), and extracted the rate of forest retreat at each point for all Type1 and Type2 polygons. We rasterized the rate samples across the region, in which the value of each grid was computed as the mean of all samples within the grid. Grids outside of polygons represent areas of no forest loss, and their values were assigned to 0. For grids inside polygons but having no rate samples, their values were interpolated as the average of surrounding grids (Fig. 6).



* For pixels inside polygons of forest loss but having no rate samplings, their values are interpolated as the average of surrounding pixels.

Fig. 6. Flowchart for spatially-explicit assessment of forest retreat rate. See text for acronym definition and detailed description of the step by step procedure.

3. RESULTS

3.1 Land surface phenology and temporal-trend analysis

Patterns of land surface phenology differ vastly between coastal vegetation types (Fig. 4 and Table 3). Specifically, six of the seven phenological metrics computed by the double-logistic filter demonstrate significant differences between vegetation types (Table 3). For example, the Start of Growing Season is estimated to be on 114 ± 5 day of year for upland forest, which is ~10 days earlier than marsh (125 ± 5) and ~20 days earlier than transition forest (135 ± 6) (Table 3).

423 Similarly, the Peak NDVI value reaches 0.82 ± 0.11 in upland forest, significantly higher than 424 surrounding vegetation of marsh (0.59 \pm 0.09) and transition forest (0.71 \pm 0.13) (Table 3). 425 The comparison of vegetation-specific NDVI trends between time-span scenarios (Fig. 5) 426 reveals that maximal inter-vegetation contrast was achieved at 24 years (i.e. the intermediate time-427 span scenario, Table 4), as indicated by the strong, significantly negative NDVI trends (P < 0.0001) 428 in transition forest, contrasted with marginally significant (P = 0.06) trends in marsh and no trend 429 at all (P = 0.84) in upland forest (Table 4). Tests of the simplistic decision tree model (Eq. (1)) 430 offer additional confirmation favoring the 24-year scenario, as the outputs of intermediate test 431 yielded the best separation of transition forest from others with an overall accuracy of 83.7%, 432 followed by 81.8% and 62.3% for the long (36 years) and short (12 years) time-span tests, 433 respectively.

Table 3. Comparison of phenological metrics between coastal vegetation. All metrics are extracted from the phenology function fitted with a double-logistic filter. Differences are tested with one-way ANOVA, and statistical significance is denoted as * $(0.01 \le P < 0.05)$, *** $(0.001 \le P < 0.01)$, *** (P < 0.001), and NS (not significant). RMSE: root mean square error.

Phonological matrice (unit) †	Land cover (mean ± SD)				
Phenological metrics (unit) †	Marsh	Transition forest	Upland forest		
Start of Growing Season (day of year) ***	125 ± 5	135 ± 6	114 ± 5		
End of Growing Season (day of year) NS	297 ± 12	300 ± 11	313 ± 8		
Peak of Growing Season (day of year) **	165 ± 10	189 ± 11	189 ± 9		
Length of Growing Season (number of days) *	172 ± 10	165 ± 12	199 ± 10		
Base NDVI (unitless) **	0.34 ± 0.07	0.54 ± 0.11	0.59 ± 0.11		
Peak NDVI (unitless) *	0.59 ± 0.09	0.71 ± 0.13	0.82 ± 0.11		
Annual Amplitude of NDVI (unitless) *	0.25 ± 0.04	0.17 ± 0.04	0.23 ± 0.03		
RMSE (N/A) NS	0.05 ± 0.01	0.04 ± 0.01	0.04 ± 0.01		
$R^2(N/A)^*$	0.83 ± 0.10	0.72 ± 0.08	0.90 ± 0.11		

†Definition of the metrics. Start of Growing Season: the day when the left edge of the fitted curve increases to 20% of the difference between the left minimum and peak NDVI; End of Growing Season: the day when the right edge of the fitted curve decreases to 20% of the difference between the right minimum and peak NDVI; Peak of Growing Season: the day when NDVI of the fitted curve reaches the maximum; Length of Growing Season: time span between the start and the end of the growing season; Base NDVI: average of the left and right minimal NDVI values of the fitted curve; Peak NDVI: maximal NDVI value of the fitted curve; Annual Amplitude of NDVI: difference between the peak and the base NDVI values.

Table 4. Comparison of trend analyses between different time-span tests. All statistics are derived from the model fitted with peak growing-season NDVI time-series. Significance is denoted as * $(0.01 \le P < 0.05)$, ** $(0.001 \le P < 0.01)$, *** (P < 0.001), and NS (not significant).

Time snan	Statistical matrice	Land cover				
Time-span	Statistical metrics	Marsh	Transition forest	Upland forest		
26	<i>Slope</i> (× 10 ⁻³)	-1.3	-4.1	0.5		
36 years (1984-2020)	$R^2{}_{adj}$	0.32	0.78	0.10		
(1704-2020)	P	3E-04 ***	3E-13 ***	$0.06~^{ m NS}$		
24	Slope (× 10 ⁻³)	-1.1	-5.7	0.1		
24 years (1996-2020)	R^2_{adj}	0.14	0.83	0.002		
(1990-2020)	P	$0.06^{\mathrm{\ NS}}$	2E-14 ***	$0.84~^{ m NS}$		
12	Slope (× 10^{-3}) R^2_{adj}	1.8	-5.1	-0.08		
12 years	R^2_{adj}	0.16	0.44	0.0005		
(2008-2020)	P	0.18^{NS}	0.013 *	0.94 $^{ m NS}$		
NDVI by the e	NDVI by the end of observation (2020) **		0.64 ± 0.07	0.81 ± 0.05		

3.2 Accuracy assessment of different classification scenarios

We assessed the land cover map generated in 2020 by the S_1 algorithm – the conventional biseasonal approach – as the baseline to benchmark the performance of our phenological- and/or trend-based algorithms (S_2 - S_4). The product of S_1 has an overall classification accuracy of 86.4% and Kappa coefficient of 0.83 (Table 5). The corresponding mean *Producer's* Accuracy (PA) and *User's* Accuracy (UA) are 87.2% and 88.1%, respectively. Close examination of the confusion matrices (Table 5) reveals large discrepancy in classification accuracy between land cover types. In particular, commission and omission errors are large for transition forest (UA of 78.5%, PA of 77.3%) due to spectral confusion with marsh and upland forest (Table 5). Overall, the S_1 algorithm underestimates the area of transition forest, in which \sim 15% of transition forest is misclassified as marsh. Correspondingly, the area colonized by marsh was notably overestimated by S_1 .

The comparison between S_1 and the other three algorithms (S_2 - S_4) offers compelling evidence that incorporating phenological metrics and/or temporal-trend information significantly improves

the overall as well as vegetation-specific classification accuracy (Tables 5-6). The phenological-based algorithm of S₂ yields an overall classification accuracy of 93.2% and Kappa coefficient of 0.91 – a sizeable increase by 8% and 10% from that of S₁ (Table 5). The improvement was mainly achieved by constraining the spectral confusion between transition forest and its surrounding vegetation of marsh and upland forest (Table 5). Specifically, the UA of transition forest increases from less than 80% in S₁ to 91.2% in S₂, and the PA increases by a similar margin from 77.3% in S₁ to 90% in S₂ (Table 5). To a lesser extent, the UA and PA of upland forest and marsh also grow appreciably from S₁ between 82.6% and 88.9% to S₂ between 91.6 and 95.6% (Table 5).

As compared to the phenological-based algorithm of S₂, the trend-based algorithm of S₃ is less effective in differentiating between land cover types (Table 5) although no statistical difference is found between the two algorithms (Table 6). The overall classification accuracy and Kappa coefficient of S₃ are respectively 5% and 7% higher than S₁, but 2% and 3% lower than S₂ (Table 5). Similar to S₁, the spectral confusion with marsh remains the largest source of omission and commission errors for transition forest in S₃ (Table 5). Nonetheless, the UA and PA of transition forest in S₃ increase considerably from S₁ by 11% and 14% – a result only 4% (UA) and 2% (PA) lower than that of S₂ (Table 5). Similarly, the UA and PA of upland forest and marsh in S₃ also show a noticeable increase by 3-9% from S₁ (Table 5).

Consistent with our expectation, the phenological- and trend-based algorithm of S₄ has the best performance among all. The S₄ algorithm achieves an overall classification accuracy of 94.1% and Kappa coefficient of 0.93 (Table 5). Although the result of S₄ is not statistically different from that of S₂, it significantly improves from that of S₃ (Table 6). Moreover, S₄ demonstrates consistently high classification accuracy among land cover types with a mean UA of 94.2% and mean PA of

93.5% (Table 5). Albeit small, S_4 offers additional improvement in the UA (91.6%) and PA (91.3%) of transition forest from that of S_2 (UA of 91.2%, PA of 90.0%) (Table 5). Concurrently, the UA and PA of upland forest and marsh (92.8-95.7%) also exhibit slight enhancement from that of S_2 (91.6-95.6%) (Table 5).

Table 5. Confusion matrix comparing classification accuracy between land cover maps generated by different algorithms/scenarios in 2020.

3.7		Reference data					*** •	
Mapping Scenarios	Land cover	Upland	Transition	Marsh	Water	Other	Other	User's accuracy
Scenarios		forest	forest	IVIAI SII	water	(Agriculture)	(Urban area)	accuracy
	Upland forest	273	20	2	0	11	1	88.9%
Sı: Bi-	Transition forest	30	245	23	2	10	2	78.5%
	Marsh	1	45	270	5	4	2	82.6%
seasonal	Water	0	3	6	220	1	1	95.2%
	Other (Agriculture)	11	3	3	6	182	1	88.3%
approach	Other (Urban area)	1	1	1	0	0	56	94.9%
	Producer's accuracy	86.4%	77.3%	88.5%	94.4%	87.5%	88.9%	
			Overall acc	euracy = 86	6.4%; Kap _l	pa coefficient = 0	.83	
	Upland forest	285	9	2	0	8	1	93.4%
	Transition forest	10	271	8	2	6	0	91.2%
S ₂ : S ₁ +	Marsh	0	15	296	7	4	1	91.6%
phenological	Water	1	4	3	233	2	1	95.5%
metrics	Other (Agriculture)	2	1	3	2	167	0	95.4%
meures	Other (Urban area)	0	1	0	2	0	47	94.0%
	Producer's accuracy	95.6%	90.0%	94.9%	94.7%	89.3%	94.0%	
			Overall acc	euracy = 93	3.2%; Kap _l	pa coefficient = 0	.91	
	Upland forest	278	11	2	0	12	1	91.4%
	Transition forest	12	266	14	1	9	2	87.5%
S ₃ : S ₁ +	Marsh	2	21	283	6	3	0	89.8%
trend	Water	0	2	6	198	2	1	94.7%
analysis	Other (Agriculture)	2	2	3	5	199	0	94.3%
allalysis	Other (Urban area)	1	0	3	2	0	48	88.9%
	Producer's accuracy	94.2%	88.1%	91.0%	93.4%	88.4%	92.3%	
	Overall accuracy = 91.1%; Kappa coefficient = 0.88							
S ₄ : S ₁ + phenological	Upland forest	267	9	0	0	6	3	93.7%
	Transition forest	9	283	7	0	9	1	91.6%
	Marsh	2	13	282	4	1	2	92.8%
	Water	0	2	3	209	0	0	97.7%
metrics +	Other (Agriculture)	1	2	2	1	194	0	97.0%
trend	Other (Urban area)	0	1	2	0	1	50	92.6%
analysis	Producer's accuracy	95.7%	91.3%	95.3%	97.7%	91.9%	89.3%	
		Overall accuracy = 94.1%; Kappa coefficient =0.93						

Table 6. Comparison of different classification scenarios using the McNemar's Chi-squared test. Refer to the text for detailed definition of the four classification scenarios (S_1 , S_2 , S_3 and S_4). Significance is denoted as * $(0.01 \le P < 0.05)$, ** $(0.001 \le P < 0.01)$, *** (P < 0.001), and NS (not significant).

Pairwise comparison		McNen	nar's Chi-squared t	test
Pairwise C	comparison	Degree of freedom	χ^2	P
S_1	S_2	1	12.37	0.0004 ***
	S_3	1	9.66	0.002 **
	S_4	1	18.18	2.0e-05 ***
S_2	S_3	1	3.82	0.051
	S_4	1	0.74	0.390
S_3	S_4	1	5.07	0.024 st

3.3 Multi-period maps and comparison with existing products

In spite of extra benefits conferred by temporal-tend information to coastal forest mapping (S₄), we selected the phenological-based algorithm of S₂ as the most suitable approach for our time-series mapping, considering that (1) the results of S₂ achieve remarkable classification accuracy with no statistical difference from that of S₄ (Tables 5-6), and (2) more critically, trend analysis required for S₄ is not applicable (24 years NDVI time-series, Table 4) for historical mapping in 1985 and 2000.

We mapped regional land cover in 1985, 2000 and 2020 using the S₂ algorithm and compared the results between time steps (Fig. 7). Similar to the results in 2020 (Table 5), the maps generated in 1985 and 2000 attain comparably high overall classification accuracy (92.1% in 1985, 94.0% in 2000) and Kappa coefficient (0.89 in 1985, 0.92 in 2000) (Fig. 7). The mean UA and PA of the map in 1985 (92.3%, 92.2%) and 2000 (94.1%, 94.0%) rival that in 2020 (93.5%, 93.1%) (Fig. 7). As illustrated by the zoomed-in sites in Figs. 8-10 (Site 1 and Site 2), our maps of coastal land

As illustrated by the zoomed-in sites in Figs. 8-10 (Site 1 and Site 2), our maps of coastal land cover in 2000 and 2020 agree well with the spatial pattern revealed by high-resolution aerial photos (0.6 m) acquired in the region. More importantly, the temporal pattern of coastal vegetation change

demonstrated by the differenced maps (Figs. 9-10) accords closely with our field observations that accelerating SLR leads to expansive mash inundation and coastal forest mortality (Figs. 2-3). In particular, we found that the marsh-forest boundary retreated as much as 1.1 km from 2000 to 2020 in Site 2, equivalent to an annual retreat rate of 55 m yr⁻¹ (Fig. 8).

Our results strikingly contrast with those derived from existing map products (C-CAP, NLCD), which indicate opposite trajectory of coastal vegetation change (marsh converted to forest), even in areas of massive forest loss highlighted in Site 2 (Figs. 9-10). As a result, the overall classification accuracy of C-CAP and NLCD products is less than 62% in our study region. Close inspection suggests that the confusion between marsh and forest is considerable in the C-CAP and NLCD products, most pronounced in areas identified as transition forest, although the degree of confusion varies between time steps (Figs. 9-10).

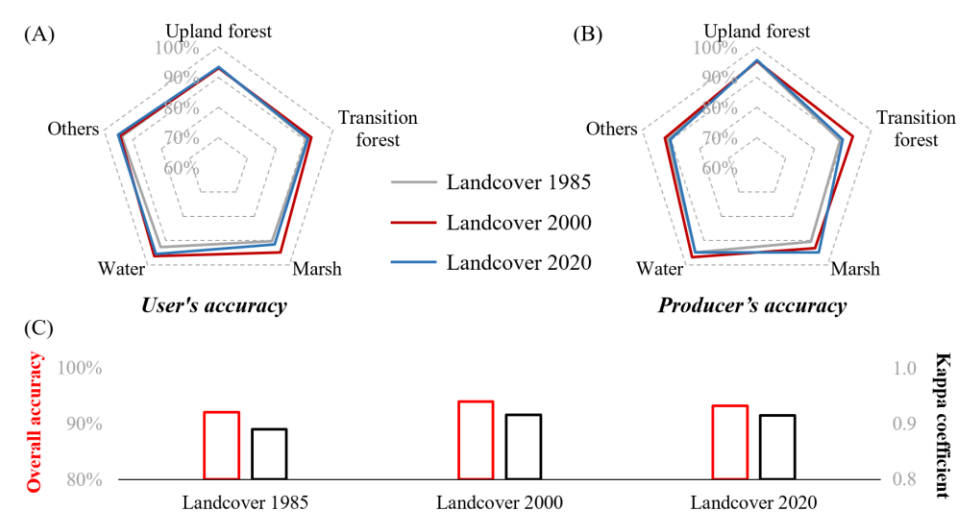


Fig. 7. Accuracy assessment shown as User's accuracy (A), Producer's accuracy (B), and Overall and Kappa coefficient (C) for the land cover maps generated by the S_2 algorithm at three time-steps (1985, 2000 and 2020).

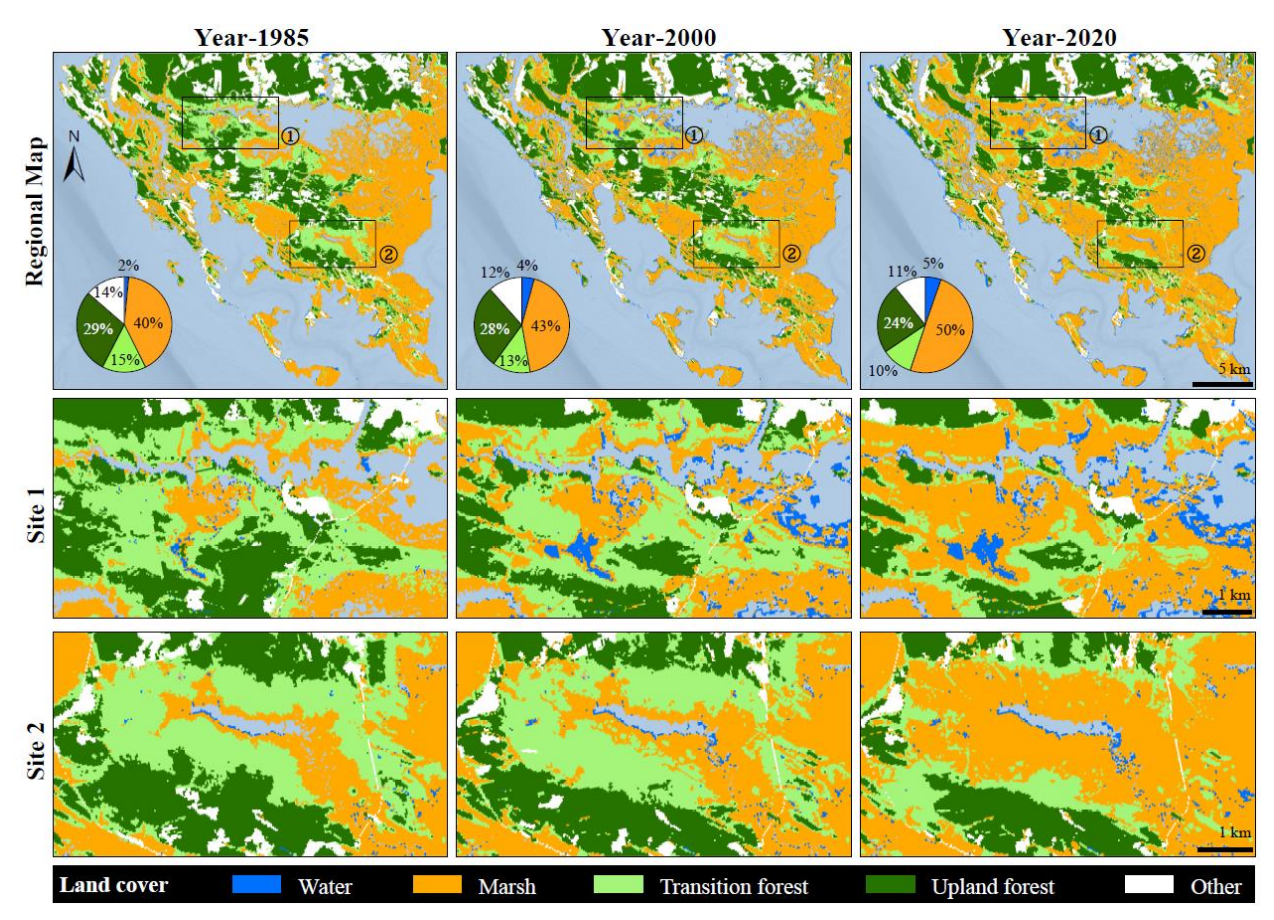


Fig. 8. Multi-period land cover maps in the study region. The inserted pie charts show the areal percentage of each land cover in the region, and the black boxes (1) and (2)) refer to the two zoom-in sites presented in detail by the second (Site 1) and third row (Site 2).

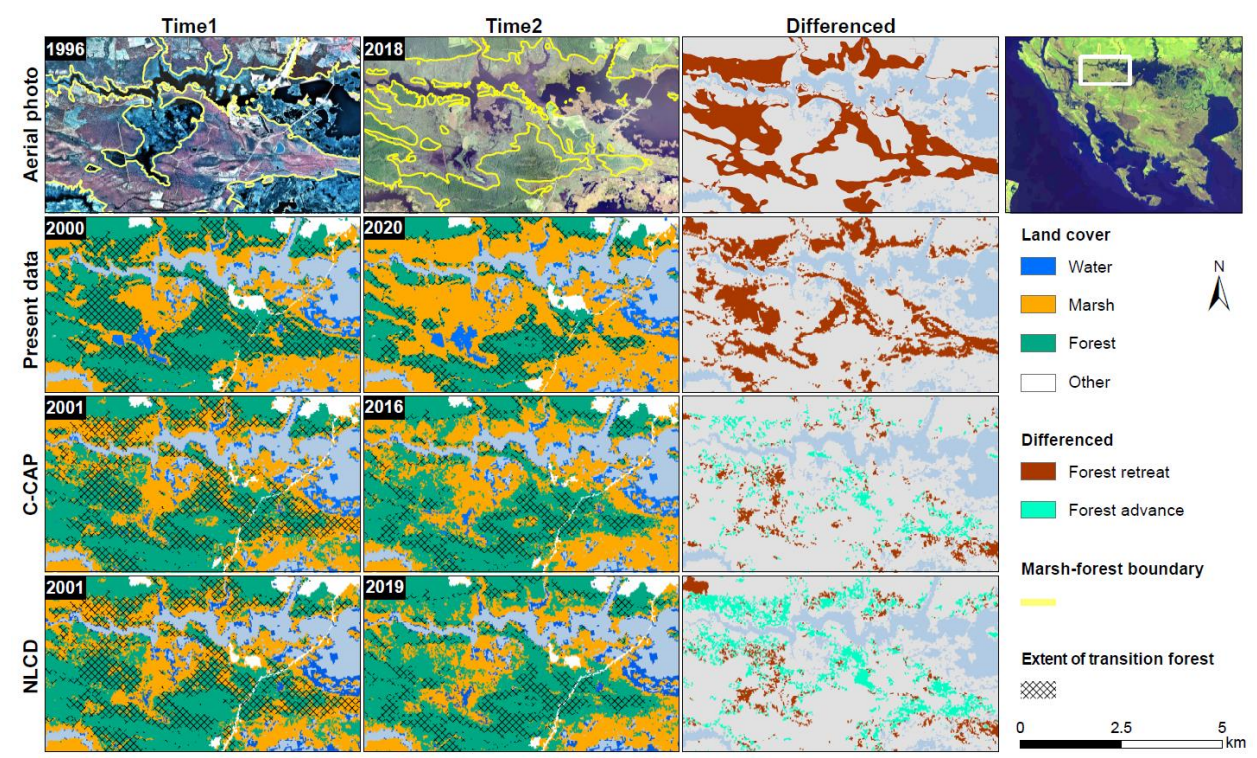


Fig. 9. Comparison of different land cover products in Site 1. The maps presented in the first row were derived from high-resolution (~1 m) aerial photos, serving as the reference for comparison. The marshforest boundary (yellow lines) was manually delineated on the aerial photos, and the differenced maps show the areal changes of coastal forest from Time1 to Time2. Our own maps generated in 2000 and 2020 were plotted in the second row. The corresponding C-CAP and NLCD products were shown in the third and fourth rows, overlaid with black lines indicating areas of transition forest identified by our products.

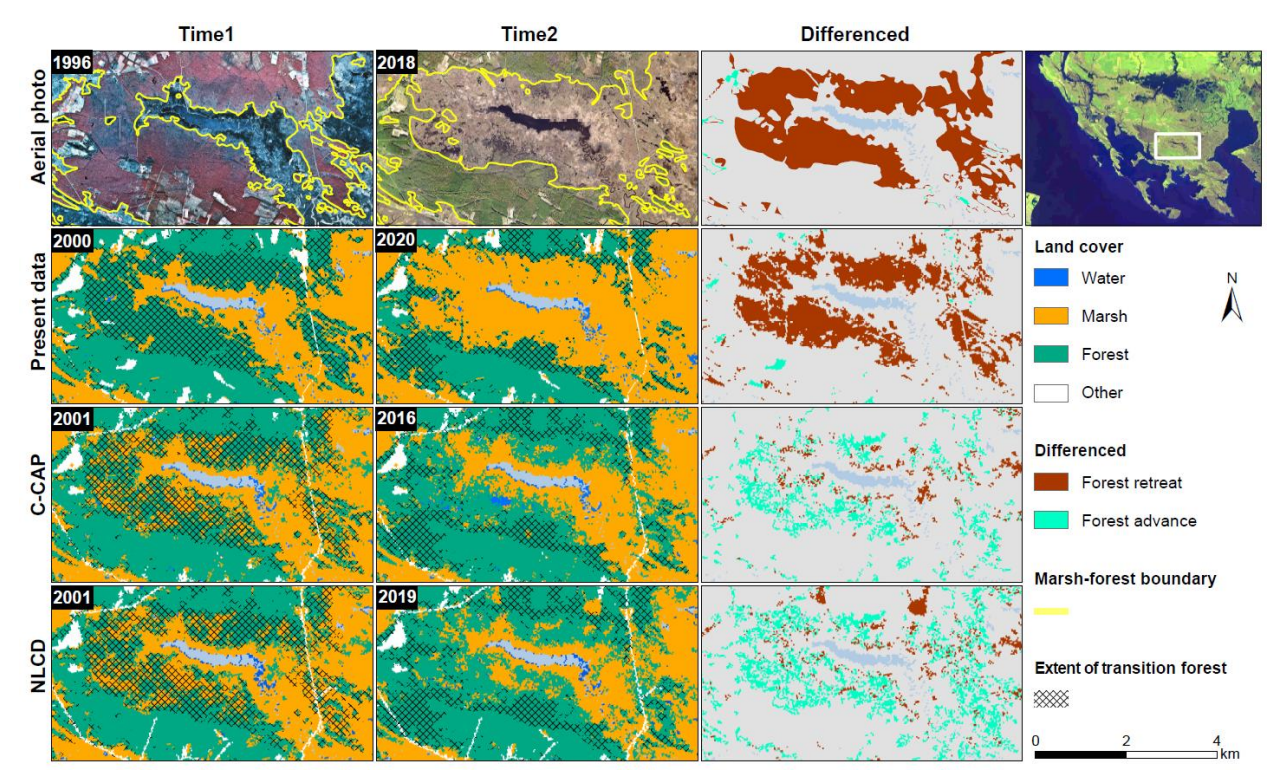


Fig. 10. Comparison of different land cover products in Site 2. The maps presented in the first row were derived from high-resolution (~1 m) aerial photos, serving as the reference for comparison. The marshforest boundary (yellow lines) was manually delineated on the aerial photos, and the differenced maps show the areal changes of coastal forest from Time1 to Time2. Our own maps in 2000 and 2020 were plotted in the second row. The corresponding C-CAP and NLCD products were shown in the third and fourth rows, overlaid with black lines indicating areas of transition forest identified by our products.

3.4 Spatiotemporal patterns of coastal vegetation change

Our time-series maps manifest that coastal vegetation change is spatially and temporally heterogenous (Figs. 8-12). From 1985 to 2000, as much as 1.23×10^3 ha of marsh was lost to open water. Meanwhile, 1.91×10^3 ha of coastal forest (1.73×10^3 ha transition forest, 1.80×10^2 ha upland forest) was converted to marsh that collectively led to an increase of marsh area by 8.75×10^2 ha (Fig. 8). Concurrently, the total forest area decreased by 5.6% from 2.09×10^4 ha in 1985

 $(7.14 \times 10^3 \text{ ha transition forest}, 1.38 \times 10^4 \text{ ha upland forest}) \text{ to } 1.97 \times 10^4 \text{ ha in } 2000 \text{ } (6.15 \times 10^3 \text{ ha transition forest}, 1.36 \times 10^4 \text{ ha upland forest}) \text{ (Fig. 8)}.$

The areal change of marsh and forest was accompanied by the systematic shift of coastal vegetation distribution along elevation gradient (Fig. 11). To be clear, the estimated elevation change of marsh and forest refers to the positional shift of vegetation distribution along the CoNED DEM, rather than in-situ elevation gain associated with vertical sedimentation. Specifically, the elevation of marsh, transition forest and upland forest respectively increased by 11 mm (from 0.29 \pm 0.20 to 0.30 \pm 0.19 m), 14 mm (from 0.35 \pm 0.16 to 0.37 \pm 0.15 m), and 40 mm (from 0.78 \pm 0.52 to 0.82 \pm 0.52 m) from 1985 to 2000 (Fig. 11). The estimated rate of marsh-forest boundary change (or horizontal forest retreat rate) was 3.07 \pm 2.79 m yr⁻¹ between 1985 and 2000 when averaged across all areas within 2 m above sea level (Fig. 12).

The comparison of vegetation change between 1985-2000 and 2000-2020 reveals that coastal landscape reorganization accelerated over time (Figs. 11-12). The area of marsh increased by 15.8% (3.25 × 10³ ha) and forest area decreased by 17.3% (1.16 × 10³ ha loss of transition forest, 2.26 × 10³ ha loss of upland forest) from 2000 to 2020 (Fig. 8). The result is equivalent to an annual marsh gain of 162.7 ha and annual forest loss of 170.9 ha, an amount more than double that during 1985-2000 (marsh gain of 58.4 ha yr⁻¹, forest loss of 78.1 ha yr⁻¹). Similar to that observed during 1985-2000, the average elevation of coastal vegetation also increased from 2000 to 2020, by 12 mm, 56 mm, and 85 mm for marsh, transition forest and upland forest, respectively (Fig. 11). Unlike marsh that exhibited comparable rates of vertical migration between 1985-2000 (0.69 mm yr⁻¹) and 2000-2020 (0.64 mm yr⁻¹), the rates of transition forest (from 0.87 to 2.94 mm yr⁻¹) and upland forest (from 2.50 to 4.49 mm yr⁻¹) largely increased from 1985-2000 to 2000-2020

(Fig. 11). Similarly, the rate of marsh-forest boundary change (i.e. horizontal forest retreat rate) increased by 52% from 1985-2000 (Fig. 12B) to 4.68 ± 3.72 m yr⁻¹ during 2000-2020 (Fig. 12C). After studying patterns of coastal forest loss (Fig. 6), we found that it is common for new marsh to establish within forest interior (number of emerging marsh patches = 809 from 1985 to 2000, and 512 from 2000 to 2020). However, the emerging marsh patches are usually small in size (0.22 \pm 0.17 ha between 1985-2000, 0.27 \pm 0.19 ha between 2000-2020), and account only for a fraction of total forest loss to marsh (9% between 1985-2000, 4% between 2000-2020). Hence, the replacement of degrading forest by expanding marsh along forest perimeter remains the predominant pathway of coastal transgression, responsible for over 90% of all forest loss to marsh from 1985 to 2020 (Figs. 11-12).

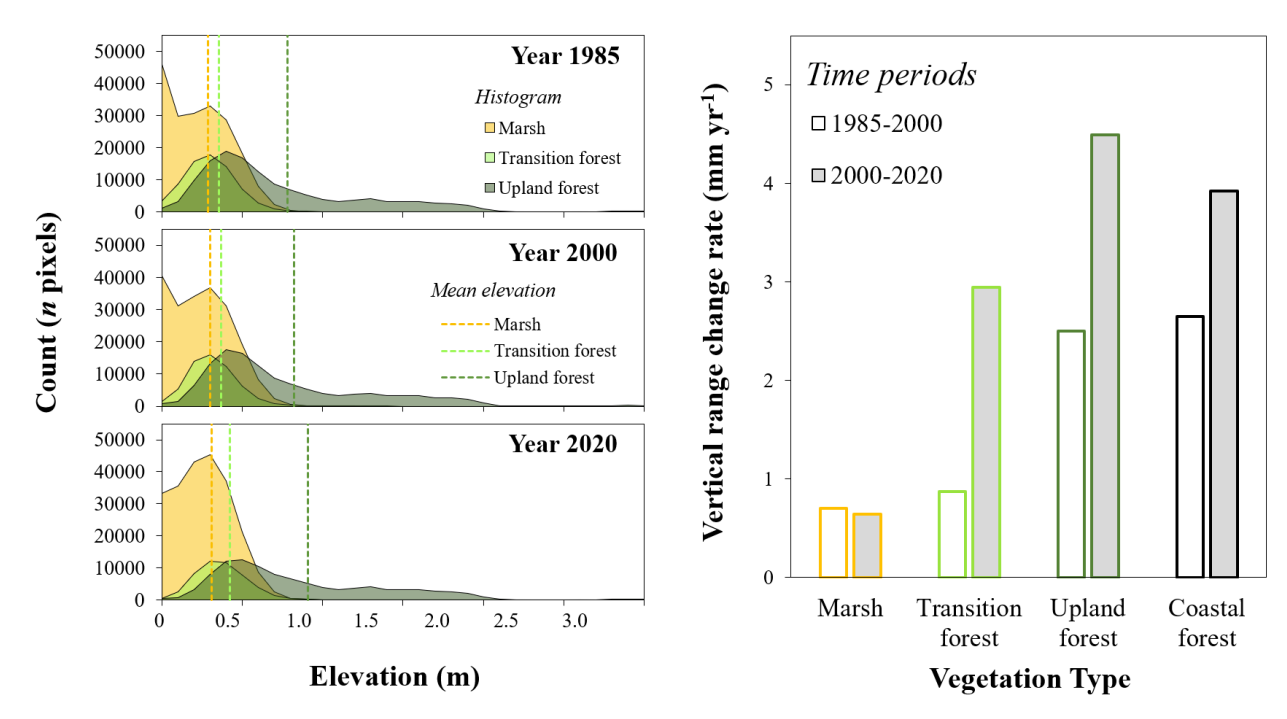


Fig. 11. Vertical range shifts of different coastal vegetation over time. Panels on the left represent the distribution histogram of each vegetation type with elevation, and the vegetation-specific mean elevation is indicated by the dotted lines. The right panel shows the vertical migration rate estimated for each vegetation type between 1985 and 2000, and between 2000 and 2020. Coastal forest is the aggregate of transition forest and upland forest.

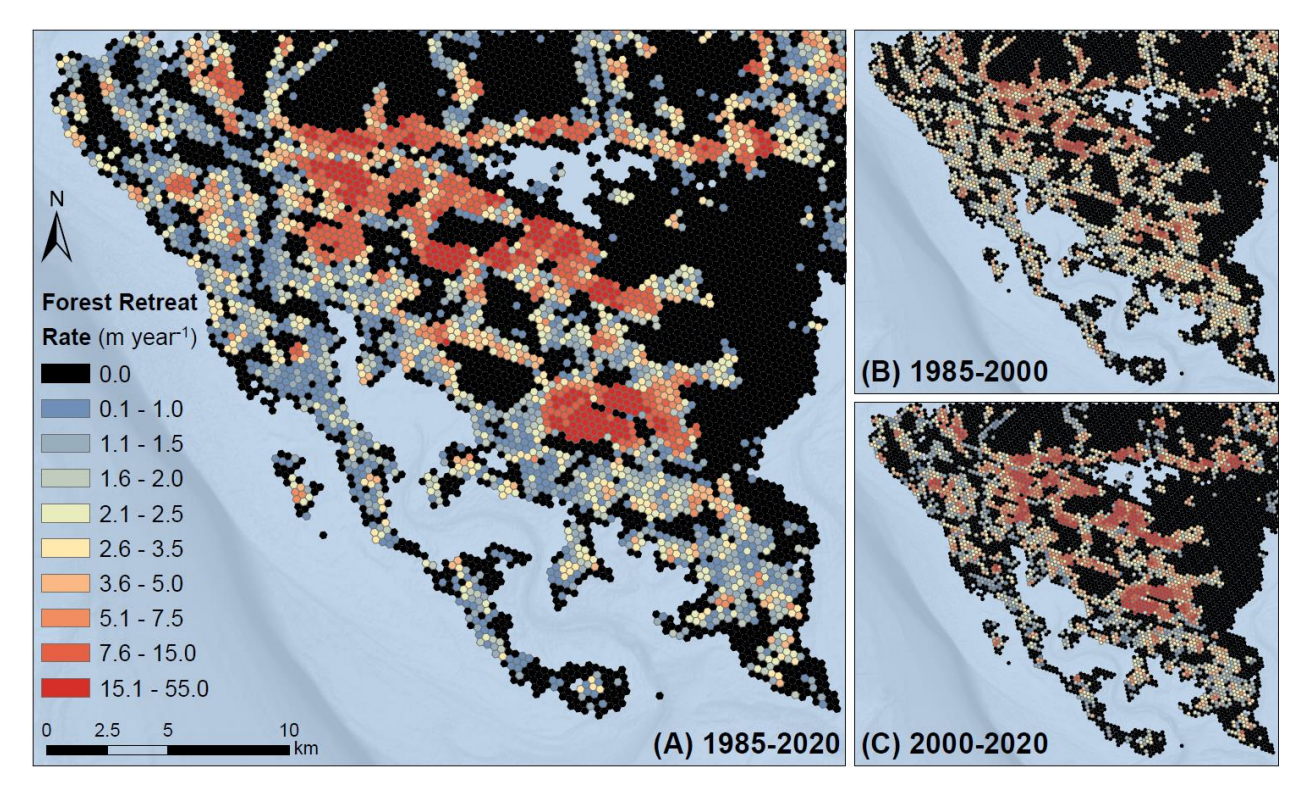


Fig. 12. Estimated horizontal forest retreat rates between 1985 and 2020 (A), between 1985 and 2000 (B), and between 2000 and 2020 (C) across our study region. Please refer to the text for a detailed description of the methodology (2.8 Spatially explicit quantification of forest retreat rate).

4. DISCUSSION

The acceleration of global SLR creates growing demand for timely and accurate monitoring of coastal landscape dynamics that is critical to sustainable ecosystem management (Hinkel et al., 2015; Oppenheimer et al., 2019). Our study developed a phenology- and trend-based algorithm that uniquely targets the ecologically-distinct transition forest to enable spatially and temporally consistent tracking of coastal transgression. The approach, in combination with our spatial analysis workflow (Fig. 6), provides a practical framework that may be integrated into cloud-based platforms such as Google Earth Engine in future efforts to allow automatic, near real-time estimates of SLR-driven forest retreat on national to global scales.

Previous studies generally suggest that algorithms combining multiple sources of information boost classification accuracy over those relying solely upon spectral information (Diao and Wang, 2016; Fagan et al., 2018; Thomas et al., 2021). We analyzed the spectral, phenological and temporal signatures of different coastal vegetation, and the results confirm the complementary contribution of different information to optimizing land cover mapping. In particular, six out of the seven phenological metrics show significant difference between transition forest and the spectrally-similar surroundings, implying systematical deviation of land surface phenology in salt-stressed forests from adjacent marsh and intact forest. Accordingly, the approach accommodating the phenological distinctions of coastal vegetation allows superior mapping accuracy to that derived from the traditional bi-seasonal approach, a result in line with earlier findings that suggest land surface phenology playing an important role in constraining intra-class variations in spatially complex landscapes (Diao and Wang, 2018, 2016; Thomas et al., 2021).

While remote sensing products can be used to facilitate a mechanistic understanding of coastal transgression (Schieder et al., 2018; Smart et al., 2020), the ecological understanding of coastal transgression in turn offers invaluable insights into advancing the remote sensing of shifting vegetation. Our temporal-trend analyses, built upon ecological theory of stressed ecosystems and ecosystems undergoing regime shifts (Carpenter et al., 2011; Chen et al., 2022; Scheffer et al., 2015), corroborate field-based studies (Smith and Kirwan, 2021; Walters et al., 2021) showing directional changes of biomass/productivity in salt-stressed forests (Fig. 5). By incorporating the temporal-tend information, our algorithm (S₄) further reduced the confusion between transition forest and the adjacent marsh and upland forest, yielding additional discriminatory power to the phenology-based approach.

It is worth noting that the strength of trend analysis depends on the temporal length of time-series data. An intermediate time-span of 24 years is identified as optimal for isolating transition forest, and a simple decision tree model (Eq. (1)) attains an overall classification accuracy beyond 80%. Given its efficacy in distinguishing transition forest, the temporal-trend analysis may be informative for other remote-sensing applications in coastal ecosystems, such as detecting early warning signals of seawater intrusion (White and Kaplan, 2021), identifying hotspots of coastal transgression, or guiding the selection of reference sites in data-limited areas for regional mapping. Moreover, as climate warming is driving worldwide intensification of press and pulse stressors (Y.-P. Chen and Ye, 2014; Chen et al., 2021b, 2020; Lara et al., 2021), similar trend-based algorithms may be applicable to other rapidly-changing ecosystems (Chen et al., 2015; Myers-Smith et al., 2015, 2011) for enhanced quantification of earth system transition.

Our time-series land cover maps in 1985, 2000 and 2020 reveal increasing rates of coastal transgression, concurrent with observed acceleration of global SLR over past decades (Dangendorf et al., 2019). This finding accords well with a number of observations in the US Atlantic coast, reporting escalated forest mortality and marsh encroachment in the recent past (Kirwan and Gedan, 2019; Miller et al., 2021; Schieder et al., 2018). Notably, we found that forest retreat rate (or landward marsh migration rate) can reach up to 55 m yr⁻¹ in some areas (Site 2), which is the fastest rate ever recorded (Kirwan and Gedan, 2019; Schieder et al., 2018; Schieder and Kirwan, 2019; Smith, 2013). Previous studies suggest that low-lying, gently-sloping terrain is conducive for marsh migration (Molino et al., 2022; Schieder and Kirwan, 2019). The extremely low relief terrain of Site 2 (mean elevation of 0.32 m, mean slope of 0.03) likely explains the exceptional rate of forest retreat, where slight increases of sea level can push saltwater far inland.

Moreover, the close comparison of the C-CAP/NLCD products to ours (Figs. 9-10) indicates that previous studies using existing maps (Gittman et al., 2019; Holmquist et al., 2018; White et al., 2021) might underestimate the vulnerability of coastal ecosystems to SLR. Although the C-CAP/NLCD time-series have been proven effective in capturing broad-scale patterns (Byrd et al., 2018; Thomas et al., 2021), these datasets may not be well suited to quantitative study of SLR-driven landscape reorganization, especially considering that forest gain is suggested in areas where we observed forest loss among the most drastic on earth (Site 2). Previous work highlighted substantial omission and commission errors for other land cover types in the C-CAP/NLCD products, especially in early maps (e.g. 2001, 2006) (Danielson et al., 2016; Fagan et al., 2018). Hence, reevaluation of the risks posed by SLR to coastal ecosystems and society is needed, and our approach may serve as a reproducible solution to ensure the spatially and temporally consistent mapping required for such assessments.

Finally, we analyzed unique patterns of coastal forest loss, and devised a practical workflow for semi-automatic creation of coastal forest retreat maps (Figs. 6 and 12). The maps generated from differenced land cover products allow spatially explicit comparison of forest retreat rates over time. The spatially explicit fashion of the forest retreat map also means that it can be analyzed with other geospatial datasets (e.g. DEM, gridded climate data) to link potential environmental drivers to dynamic coastal transgression. Importantly, the spatial analysis workflow developed here is not limited to studying coastal forest change, it may be generalized to tackle other environmental processes and hazards involving positional changes over time, such as coastal land loss (Hurst et al., 2016; Roy et al., 2020), northern shrubline/treeline advance (Elmendorf et al., 2012; Sturm et al., 2001), or landslide progress (Balser et al., 2014; Li et al., 2022). Taken together,

our spatial analysis method may be a useful addition in a diversity of future applications in support of natural resource management, and risk assessment and mitigation.

5. CONCLUSION

We developed a phenology- and trend-based algorithm in this study to track coastal vegetation change with high precision and consistency. Our approach significantly improves the classification accuracy of salt-impacted coastal forest over existing map products, and the results reveal a striking rate of coastal transgression over the past four decades that was underestimated in existing remote sensing products (i.e. C-CAP, NLCD). The predicted intensification of climate change will result in a growing need for rapid and spatially explicit measures of global landscape reorganization, and our study offers a viable solution to evaluate coastal vegetation change in a regionally consistent and locally relevant fashion. With the growing power of cloud-based technology represented by Google Earth Engine, it is possible to automate our approach in future efforts to allow real-time estimates on the status and trends of SLR-driven coastal transgression worldwide.

692 **Declaration of Competing Interest** 693 The authors declare that they have no known competing financial interests or personal 694 relationships that could have appeared to influence the work reported in this paper. 695 **Author contributions** 696 Y.C. designed the study, performed the analysis, and wrote the initial draft. M.L.K conceived the 697 idea, contributed to the study design and revised the manuscript. All authors interpreted the data. 698 Acknowledgements 699 Primary funding for this work comes from the National Science Foundation (#1654374, 1832221, 700 and 2012670) with additional support from the US Department of Energy, Office of Biological 701 and Environmental Research Program (DE-SC0021112). Tyler Messerschmidt and Alex Smith 702 helped with field work. This is contribution xxxx of the Virginia Institute of Marine Science,

703

704

William & Mary.

REFERENCES

705

717

718

719

723

724

725

726

727

728

729

730

733

734

738

739

740

741

- Atkinson, P.M., Jeganathan, C., Dash, J., Atzberger, C., 2012. Inter-comparison of four models for smoothing satellite sensor time-series data to estimate vegetation phenology. Remote Sens. Environ. 123, 400–417. https://doi.org/10.1016/j.rse.2012.04.001
- Balser, A.W., Jones, J.B., Gens, R., 2014. Timing of retrogressive thaw slump initiation in the
 Noatak Basin, northwest Alaska, USA. J. Geophys. Res. Earth Surf. 119, 1106–1120.
 https://doi.org/10.1002/2013JF002889
- Bégin, Y., 1990. The Effects of Shoreline Transgression on Woody Plants, Upper St. Lawrence
 Estuary, Québec. J. Coast. Res. 6, 815–827.
- Belgiu, M., Csillik, O., 2018. Sentinel-2 cropland mapping using pixel-based and object-based time-weighted dynamic time warping analysis. Remote Sens. Environ. 204, 509–523. https://doi.org/10.1016/j.rse.2017.10.005
 - Belgiu, M., Drăgu, L., 2016. Random forest in remote sensing: A review of applications and future directions. ISPRS J. Photogramm. Remote Sens. 114, 24–31. https://doi.org/10.1016/j.isprsjprs.2016.01.011
- Berner, L.T., Jantz, P., Tape, K.D., Goetz, S.J., 2018. Tundra plant above-ground biomass and shrub dominance mapped across the North Slope of Alaska. Environ. Res. Lett. 13. https://doi.org/10.1088/1748-9326/aaaa9a
 - Berner, L.T., Massey, R., Jantz, P., Forbes, B.C., Macias-Fauria, M., Myers-Smith, I., Kumpula, T., Gauthier, G., Andreu-Hayles, L., Gaglioti, B. V., Burns, P., Zetterberg, P., D'Arrigo, R., Goetz, S.J., 2020. Summer warming explains widespread but not uniform greening in the Arctic tundra biome. Nat. Commun. 11, 4621. https://doi.org/10.1038/s41467-020-18479-5
 - Bhattachan, A., Jurjonas, M.D., Moody, A.C., Morris, P.R., Sanchez, G.M., Smart, L.S., Taillie, P.J., Emanuel, R.E., Seekamp, E.L., 2018. Sea level rise impacts on rural coastal social-ecological systems and the implications for decision making. Environ. Sci. Policy 90, 122–134. https://doi.org/10.1016/j.envsci.2018.10.006
- 731 Breiman, L., 2001. Random Forests. Mach. Learn. 45, 5–32. 732 https://doi.org/https://doi.org/10.1023/A:1010933404324
 - Bronaugh, D., Werner, A., 2019. zyp: Zhang + Yue-Pilon Trends Package Version 0.10-1.1 [WWW Document]. URL https://cran.r-project.org/web/packages/zyp/index.html
- Brooks, E.B., Thomas, V.A., Wynne, R.H., Coulston, J.W., 2012. Fitting the multitemporal curve:
 A fourier series approach to the missing data problem in remote sensing analysis. IEEE Trans.
 Geosci. Remote Sens. 50, 3340–3353. https://doi.org/10.1109/TGRS.2012.2183137
 - Byrd, K.B., Ballanti, L., Thomas, N., Nguyen, D., Holmquist, J.R., Simard, M., Windham-Myers, L., 2018. A remote sensing-based model of tidal marsh aboveground carbon stocks for the conterminous United States. ISPRS J. Photogramm. Remote Sens. 139, 255–271. https://doi.org/10.1016/j.isprsjprs.2018.03.019
- Campbell, A.D., Wang, Y., 2020. Salt marsh monitoring along the mid-Atlantic coast by Google
 Earth Engine enabled time series. PLoS One 15, e0229605.
 https://doi.org/10.1371/journal.pone.0229605
- Carpenter, S.R., Cole, J.J., Pace, M.L., Batt, R., Brock, W.A., Cline, T., Coloso, J., Hodgson, J.R.,
 Kitchell, J.F., Seekell, D.A., Smith, L., Weidel, B., 2011. Early Warnings of Regime Shifts:
 A Whole-Ecosystem Experiment. Science (80-.). 332, 1079–1082.

748 https://doi.org/10.1126/science.1203672

- 749 Chen, Y.-P., Ye, Y., 2014. Early responses of Avicennia marina (Forsk.) Vierh. to intertidal 750 elevation and light level. Aquat. Bot. 112, 33–40. 751 https://doi.org/10.1016/j.aquabot.2013.07.006
- 752 Chen, Y., Chen, G., Ye, Y., 2015. Coastal vegetation invasion increases greenhouse gas emission 753 from wetland soils but also increases soil carbon accumulation. Sci. Total Environ. 526, 19– 754 28. https://doi.org/10.1016/j.scitotenv.2015.04.077
- Chen, Y., Hu, F.S., Lara, M.J., 2021a. Divergent shrub-cover responses driven by climate, wildfire,
 and permafrost interactions in Arctic tundra ecosystems. Glob. Chang. Biol. 27, 652–663.
 https://doi.org/10.1111/gcb.15451

759

760

764

765

766

767

768

769

770

771

772

773

774

775

776

779

780

781

782

783

- Chen, Y., Kelly, R., Genet, H., Lara, M.J., Chipman, M.L., McGuire, A.D., Hu, F.S., 2022. Resilience and sensitivity of ecosystem carbon stocks to fire-regime change in Alaskan tundra. Sci. Total Environ. 806, 151482. https://doi.org/10.1016/j.scitotenv.2021.151482
- 761 Chen, Y., Lara, M.J., Hu, F.S., 2020. A robust visible near-infrared index for fire severity mapping 762 in Arctic tundra ecosystems. ISPRS J. Photogramm. Remote Sens. 159, 101–113. 763 https://doi.org/10.1016/j.isprsjprs.2019.11.012
 - Chen, Y., Lara, M.J., Jones, B.M., Frost, G. V., Hu, F.S., 2021b. Thermokarst acceleration in Arctic tundra driven by climate change and fire disturbance. One Earth 4, 1718–1729. https://doi.org/10.1016/j.oneear.2021.11.011
 - Chen, Y., Ye, Y., 2014. Effects of Salinity and Nutrient Addition on Mangrove Excoecaria agallocha. PLoS One 9, e93337. https://doi.org/10.1371/journal.pone.0093337
 - Chen, Y., Ye, Y., 2013. Growth and physiological responses of saplings of two mangrove species to intertidal elevation. Mar. Ecol. Prog. Ser. 482, 107–118. https://doi.org/10.3354/meps10274
 - Clark, J.S., 1986. Coastal Forest Tree Populations in a Changing Environment, Southeastern Long Island, New York. Ecol. Monogr. 56, 259–277. https://doi.org/10.2307/2937077
 - Dangendorf, S., Hay, C., Calafat, F.M., Marcos, M., Piecuch, C.G., Berk, K., Jensen, J., 2019. Persistent acceleration in global sea-level rise since the 1960s. Nat. Clim. Chang. 9, 705–710. https://doi.org/10.1038/s41558-019-0531-8
- Danielson, J.J., Poppenga, S.K., Tyler, D.J., Palaseanu-Lovejoy, M., Gesch, D.B., 2018. Coastal
 National Elevation Database, Fact Sheet. Reston, VA. https://doi.org/10.3133/fs20183037
 - Danielson, P., Yang, L., Jin, S., Homer, C., Napton, D., 2016. An Assessment of the Cultivated Cropland Class of NLCD 2006 Using a Multi-Source and Multi-Criteria Approach. Remote Sens. 8, 101. https://doi.org/10.3390/rs8020101
 - Diao, C., Wang, L., 2018. Landsat time series-based multiyear spectral angle clustering (MSAC) model to monitor the inter-annual leaf senescence of exotic saltcedar. Remote Sens. Environ. 209, 581–593. https://doi.org/10.1016/j.rse.2018.02.036
- Diao, C., Wang, L., 2016. Incorporating plant phenological trajectory in exotic saltcedar detection with monthly time series of Landsat imagery. Remote Sens. Environ. 182, 60–71. https://doi.org/10.1016/j.rse.2016.04.029
- 788 Eilers, P.H.C., 2003. A Perfect Smoother. Anal. Chem. 75, 3631–3636. 789 https://doi.org/10.1021/ac034173t
- Elmendorf, S.C., Henry, G.H.R., Hollister, R.D., Björk, R.G., Bjorkman, A.D., Callaghan, T. V., Collier, L.S., Cooper, E.J., Cornelissen, J.H.C., Day, T.A., Fosaa, A.M., Gould, W.A., Grétarsdóttir, J., Harte, J., Hermanutz, L., Hik, D.S., Hofgaard, A., Jarrad, F., Jónsdóttir, I.S.,

- Keuper, F., Klanderud, K., Klein, J.A., Koh, S., Kudo, G., Lang, S.I., Loewen, V., May, J.L., Mercado, J., Michelsen, A., Molau, U., Myers-Smith, I.H., Oberbauer, S.F., Pieper, S., Post, E., Rixen, C., Robinson, C.H., Schmidt, N.M., Shaver, G.R., Stenström, A., Tolvanen, A., Totland, Ø., Troxler, T., Wahren, C.H., Webber, P.J., Welker, J.M., Wookey, P.A., 2012. Global assessment of experimental climate warming on tundra vegetation: Heterogeneity over space and time. Ecol. Lett. 15, 164–175. https://doi.org/10.1111/j.1461-0248.2011.01716.x
- Fagan, M.E., Morton, D.C., Cook, B.D., Masek, J., Zhao, F., Nelson, R.F., Huang, C., 2018.

 Mapping pine plantations in the southeastern U.S. using structural, spectral, and temporal remote sensing data. Remote Sens. Environ. 216, 415–426. https://doi.org/10.1016/j.rse.2018.07.007
- Flester, J.A., Blum, L.K., 2020. Rates of Mainland Marsh Migration into Uplands and Seaward Edge Erosion are Explained by Geomorphic Type of Salt Marsh in Virginia Coastal Lagoons. Wetlands 40, 1703–1715. https://doi.org/10.1007/s13157-020-01390-6

808

809

- Gedan, K.B., Kirwan, M.L., Wolanski, E., Barbier, E.B., Silliman, B.R., 2011. The present and future role of coastal wetland vegetation in protecting shorelines: Answering recent challenges to the paradigm. Clim. Change 106, 7–29. https://doi.org/10.1007/s10584-010-0003-7
- Gittman, R.K., Baillie, C.J., Arkema, K.K., Bennett, R.O., Benoit, J., Blitch, S., Brun, J., Chatwin,
 A., Colden, A., Dausman, A., DeAngelis, B., Herold, N., Henkel, J., Houge, R., Howard, R.,
 Hughes, A.R., Scyphers, S.B., Shostik, T., Sutton-Grier, A., Grabowski, J.H., 2019.
 Voluntary Restoration: Mitigation's Silent Partner in the Quest to Reverse Coastal Wetland
 Loss in the USA. Front. Mar. Sci. 6. https://doi.org/10.3389/fmars.2019.00511
- Gong, P., Liu, H., Zhang, M., Li, C., Wang, J., Huang, H., Clinton, N., Ji, L., Li, Wenyu, Bai, Y., Chen, B., Xu, B., Zhu, Z., Yuan, C., Ping Suen, H., Guo, J., Xu, N., Li, Weijia, Zhao, Y., Yang, J., Yu, C., Wang, X., Fu, H., Yu, L., Dronova, I., Hui, F., Cheng, X., Shi, X., Xiao, F., Liu, Q., Song, L., 2019. Stable classification with limited sample: transferring a 30-m resolution sample set collected in 2015 to mapping 10-m resolution global land cover in 2017. Sci. Bull. 64, 370–373. https://doi.org/10.1016/j.scib.2019.03.002
- He, K., Zhang, Y., Li, W., Sun, G., McNulty, S., 2022. Detecting Coastal Wetland Degradation by
 Combining Remote Sensing and Hydrologic Modeling. Forests 13, 411.
 https://doi.org/10.3390/f13030411
- Hinkel, J., Jaeger, C., Nicholls, R.J., Lowe, J., Renn, O., Peijun, S., 2015. Sea-level rise scenarios and coastal risk management. Nat. Clim. Chang. 5, 188–190. https://doi.org/10.1038/nclimate2505
- Holmquist, J.R., Windham-Myers, L., Bernal, B., Byrd, K.B., Crooks, S., Gonneea, M.E., Herold, N., Knox, S.H., Kroeger, K.D., McCombs, J., Megonigal, J.P., Lu, M., Morris, J.T., Sutton-Grier, A.E., Troxler, T.G., Weller, D.E., 2018. Uncertainty in United States coastal wetland greenhouse gas inventorying. Environ. Res. Lett. 13, 115005. https://doi.org/10.1088/1748-9326/aae157
- Homer, C.G., Dewitz, J., Yang, L., Jin, S., Danielson, P., Xian, G.Z., Coulston, J., Herold, N., Wickham, J., Megown, K., 2015. Completion of the 2011 National Land Cover Database for the conterminous United States Representing a decade of land cover change information. Photogramm. Eng. Remote Sensing 81, 345–354.

- Hurst, M.D., Rood, D.H., Ellis, M.A., Anderson, R.S., Dornbusch, U., 2016. Recent acceleration in coastal cliff retreat rates on the south coast of Great Britain. Proc. Natl. Acad. Sci. 113, 13336–13341. https://doi.org/10.1073/pnas.1613044113
- Ihlen, V., Zanter, K., 2019a. Landsat 7 (L7) Data Users Handbook. LSDS-1927 Version 2.0.
 Department of the Interior, U.S. Geological Survey.
- Ihlen, V., Zanter, K., 2019b. Landsat 8 (L8) Data Users Handbook. LSDS-1574 Version 5.0.
 Department of the Interior, U.S. Geological Survey.
- Jönsson, P., Eklundh, L., 2004. TIMESAT—a program for analyzing time-series of satellite sensor data. Comput. Geosci. 30, 833–845. https://doi.org/10.1016/j.cageo.2004.05.006
- Ju, J., Masek, J.G., 2016. The vegetation greenness trend in Canada and US Alaska from 19842012 Landsat data. Remote Sens. Environ. 176, 1–16.
 https://doi.org/10.1016/j.rse.2016.01.001
- Kirwan, M.L., Gedan, K.B., 2019. Sea-level driven land conversion and the formation of ghost forests. Nat. Clim. Chang. 9, 450–457. https://doi.org/10.1038/s41558-019-0488-7
- Kirwan, M.L., Megonigal, J.P., 2013. Tidal wetland stability in the face of human impacts and sea-level rise. Nature 504, 53–60. https://doi.org/10.1038/nature12856
- Kong, D., 2020. R package: A state-of-the-art Vegetation Phenology extraction package, phenofit version 0.3.1. https://doi.org/doi:10.5281/zenodo.5150204
- Kong, D., Zhang, Y., Gu, X., Wang, D., 2019. A robust method for reconstructing global MODIS
 EVI time series on the Google Earth Engine. ISPRS J. Photogramm. Remote Sens. 155, 13–
 https://doi.org/10.1016/j.isprsjprs.2019.06.014
- Kuhn, M., Wing, J., Weston, S., Williams, A., Keefer, C., Engelhardt, A., Cooper, T., Mayer, Z., Kenkel, B., Benesty, M., 2021. caret: Classification and Regression Training. R Core Team.

861

- Kulp, S.A., Strauss, B.H., 2019. New elevation data triple estimates of global vulnerability to sealevel rise and coastal flooding. Nat. Commun. 10, 4844. https://doi.org/10.1038/s41467-019-12808-z
- Lara, M.J., Chen, Y., Jones, B.M., 2021. Recent warming reverses forty-year decline in catastrophic lake drainage and hastens gradual lake drainage across northern Alaska. Environ. Res. Lett. 16, 124019. https://doi.org/10.1088/1748-9326/ac3602
- Li, N., Tang, C., Yang, T., 2022. Ten years of landslide development after the Wenchuan earthquake: a case study from Miansi town, China. Nat. Hazards. https://doi.org/10.1007/s11069-021-05157-y
- Liaw, A., Wiener, M., 2002. Classification and Regression by randomForest. R News 2, 18–22.
- Miller, C.B., Rodriguez, A.B., Bost, M.C., 2021. Sea-level rise, localized subsidence, and increased storminess promote saltmarsh transgression across low-gradient upland areas. Quat. Sci. Rev. 265, 107000. https://doi.org/10.1016/j.quascirev.2021.107000
- Molino, G.D., Carr, J.A., Ganju, N.K., Kirwan, M.L., 2022. Variability in marsh migration potential determined by topographic rather than anthropogenic constraints in the Chesapeake Bay region. Limnol. Oceanogr. Lett. https://doi.org/10.1002/lo12.10262
- Munns, R., Tester, M., 2008. Mechanisms of Salinity Tolerance. Annu. Rev. Plant Biol. 59, 651–681. https://doi.org/10.1146/annurev.arplant.59.032607.092911
- Myers-Smith, I.H., Elmendorf, S.C., Beck, P.S.A., Wilmking, M., Hallinger, M., Blok, D., Tape, K.D., Rayback, S.A., Macias-Fauria, M., Forbes, B.C., Speed, J.D.M., Boulanger-Lapointe, N., Rixen, C., Lévesque, E., Schmidt, N.M., Baittinger, C., Trant, A.J., Hermanutz, L.,

- Collier, L.S., Dawes, M.A., Lantz, T.C., Weijers, S., JØrgensen, R.H., Buchwal, A., Buras, A., Naito, A.T., Ravolainen, V., Schaepman-Strub, G., Wheeler, J.A., Wipf, S., Guay, K.C., Hik, D.S., Vellend, M., 2015. Climate sensitivity of shrub growth across the tundra biome. Nat. Clim. Chang. 5, 887–891. https://doi.org/10.1038/nclimate2697
- Myers-Smith, I.H., Forbes, B.C., Wilmking, M., Hallinger, M., Lantz, T., Blok, D., Tape, K.D.,
 MacIas-Fauria, M., Sass-Klaassen, U., Lévesque, E., Boudreau, S., Ropars, P., Hermanutz,
 L., Trant, A., Collier, L.S., Weijers, S., Rozema, J., Rayback, S.A., Schmidt, N.M.,
 Schaepman-Strub, G., Wipf, S., Rixen, C., Ménard, C.B., Venn, S., Goetz, S., Andreu-Hayles,
 L., Elmendorf, S., Ravolainen, V., Welker, J., Grogan, P., Epstein, H.E., Hik, D.S., 2011.
 Shrub expansion in tundra ecosystems: Dynamics, impacts and research priorities. Environ.
 Res. Lett. 6. https://doi.org/10.1088/1748-9326/6/4/045509
- NOAA Office for Coastal Management, 2016. NOAA Coastal Change Analysis Program (C-CAP)
 Regional Land Cover Database. Data collected 1995-present. Charleston, SC.

895

896

897

898

899

900

901

902

903

904

905

906

907

908

- O'Connell, J.L., Mishra, D.R., Cotten, D.L., Wang, L., Alber, M., 2017. The Tidal Marsh Inundation Index (TMII): An inundation filter to flag flooded pixels and improve MODIS tidal marsh vegetation time-series analysis. Remote Sens. Environ. 201, 34–46. https://doi.org/10.1016/j.rse.2017.08.008
- Oppenheimer, M., Glavovic, B.C., Hinkel, J., van de Wal, R., Magnan, A.K., Abd-Elgawad, A., Cai, R., CifuentesJara, M., DeConto, R.M., Ghosh, T., Hay, J., Isla, F., Marzeion, B., Meyssignac, B., Sebesvari, Z., 2019. Sea Level Rise and Implications for Low-Lying Islands, Coasts and Communities. In: IPCC Special Report on the Ocean and Cryosphere in a Changing Climate [H.-O. P rtner, D.C. Roberts, V. Masson-Delmotte, P. Zhai, M. Tignor, E. Poloczanska, K. Mintenbeck, .
- Osland, M.J., Hughes, A.R., Armitage, A.R., Scyphers, S.B., Cebrian, J., Swinea, S.H., Shepard, C.C., Allen, M.S., Feher, L.C., Nelson, J.A., O'Brien, C.L., Sanspree, C.R., Smee, D.L., Snyder, C.M., Stetter, A.P., Stevens, P.W., Swanson, K.M., Williams, L.H., Brush, J.M., Marchionno, J., Bardou, R., 2022. The impacts of mangrove range expansion on wetland ecosystem services in the southeastern United States: Current understanding, knowledge gaps, and emerging research needs. Glob. Chang. Biol. https://doi.org/10.1111/gcb.16111
- Roy, D.P., Kovalskyy, V., Zhang, H.K., Vermote, E.F., Yan, L., Kumar, S.S., Egorov, A., 2016.
 Characterization of Landsat-7 to Landsat-8 reflective wavelength and normalized difference
 vegetation index continuity. Remote Sens. Environ. 185, 57–70.
 https://doi.org/10.1016/j.rse.2015.12.024
- Roy, S., Robeson, S.M., Ortiz, A.C., Edmonds, D.A., 2020. Spatial and temporal patterns of land loss in the Lower Mississippi River Delta from 1983 to 2016. Remote Sens. Environ. 250, 112046. https://doi.org/10.1016/j.rse.2020.112046
- 917 Sallenger, A.H., Doran, K.S., Howd, P.A., 2012. Hotspot of accelerated sea-level rise on the 918 Atlantic coast of North America. Nat. Clim. Chang. 2, 884–888. 919 https://doi.org/10.1038/nclimate1597
- 920 Scheffer, M., Carpenter, S.R., Dakos, V., van Nes, E.H., 2015. Generic Indicators of Ecological 921 Resilience: Inferring the Chance of a Critical Transition. Annu. Rev. Ecol. Evol. Syst. 46, 922 145–167. https://doi.org/10.1146/annurev-ecolsys-112414-054242
- 923 Schieder, N.W., Kirwan, M.L., 2019. Sea-level driven acceleration in coastal forest retreat. Geology 47, 1151–1155. https://doi.org/10.1130/G46607.1

- 925 Schieder, N.W., Walters, D.C., Kirwan, M.L., 2018. Massive Upland to Wetland Conversion 926 Compensated for Historical Marsh Loss in Chesapeake Bay, USA. Estuaries and Coasts 41, 927 940–951. https://doi.org/10.1007/s12237-017-0336-9
- 928 Smart, L.S., Taillie, P.J., Poulter, B., Vukomanovic, J., Singh, K.K., Swenson, J.J., Mitasova, H.,
 929 Smith, J.W., Meentemeyer, R.K., 2020. Aboveground carbon loss associated with the spread
 930 of ghost forests as sea levels rise. Environ. Res. Lett. 15. https://doi.org/10.1088/1748931 9326/aba136
- 932 Smith, A.J., Kirwan, M.L., 2021. Sea Level-Driven Marsh Migration Results in Rapid Net Loss of Carbon. Geophys. Res. Lett. 48, 1–11. https://doi.org/10.1029/2021GL092420
- 934 Smith, J.A.M., 2013. The Role of Phragmites australis in Mediating Inland Salt Marsh Migration 935 in a Mid-Atlantic Estuary. PLoS One 8, e65091. 936 https://doi.org/10.1371/journal.pone.0065091
- 937 Sturm, M., Racine, C., Tape, K., 2001. Increasing shrub abundance in the Arctic. Nature 411, 546– 547. https://doi.org/10.1038/35079180
- Theil, H., 1950. A rank-invariant method of linear and polynomial regression analysis, 3; confidence regions for the parameters of polynomial regression equations. KNAW.

942

943

944

945

946

947

948

956

957

958

- Thomas, V.A., Wynne, R.H., Kauffman, J., McCurdy, W., Brooks, E.B., Thomas, R.Q., Rakestraw, J., 2021. Mapping thins to identify active forest management in southern pine plantations using Landsat time series stacks. Remote Sens. Environ. 252, 112127. https://doi.org/10.1016/j.rse.2020.112127
- Tian, J., Wang, L., Yin, D., Li, X., Diao, C., Gong, H., Shi, C., Menenti, M., Ge, Y., Nie, S., Ou, Y., Song, X., Liu, X., 2020. Development of spectral-phenological features for deep learning to understand Spartina alterniflora invasion. Remote Sens. Environ. 242, 111745. https://doi.org/10.1016/j.rse.2020.111745
- 949 Ury, E.A., Yang, X., Wright, J.P., Bernhardt, E.S., 2021. Rapid deforestation of a coastal landscape 950 driven by sea-level rise and extreme events. Ecol. Appl. 31, 1-11.951 https://doi.org/10.1002/eap.2339
- Walters, D.C., Carr, J.A., Hockaday, A., Jones, J.A., McFarland, E., Kovalenko, K.E., Kirwan,
 M.L., Cahoon, D.R., Guntenspergen, G.R., 2021. Experimental Tree Mortality Does Not
 Induce Marsh Transgression in a Chesapeake Bay Low-Lying Coastal Forest. Front. Mar.
 Sci. 8. https://doi.org/10.3389/fmars.2021.782643
 - Wang, F., Shao, W., Yu, H., Kan, G., He, X., Zhang, D., Ren, M., Wang, G., 2020. Re-evaluation of the Power of the Mann-Kendall Test for Detecting Monotonic Trends in Hydrometeorological Time Series. Front. Earth Sci. 8. https://doi.org/10.3389/feart.2020.00014
- Weis, J.S., Harman, C., Ravit, B., Watson, E., 2020. The status and future of tidal marshes in New
 Jersey faced with sea level rise. Final Report. New Jersey department of environmental
 protection science advisory board.
- White, E., Kaplan, D., 2021. Identifying the effects of chronic saltwater intrusion in coastal
 floodplain swamps using remote sensing. Remote Sens. Environ. 258, 112385.
 https://doi.org/10.1016/j.rse.2021.112385
- White, E.E., Ury, E.A., Bernhardt, E.S., Yang, X., 2021. Climate Change Driving Widespread
 Loss of Coastal Forested Wetlands Throughout the North American Coastal Plain.
 Ecosystems. https://doi.org/10.1007/s10021-021-00686-w

- White, M.A., Thornton, P.E., Running, S.W., 1997. A continental phenology model for monitoring
 vegetation responses to interannual climatic variability. Global Biogeochem. Cycles 11, 217–
 234. https://doi.org/10.1029/97GB00330
- Zhang, F., Yang, X., 2020. Improving land cover classification in an urbanized coastal area by
 random forests: The role of variable selection. Remote Sens. Environ. 251, 112105.
 https://doi.org/10.1016/j.rse.2020.112105
- Zhang, X., Xiao, X., Qiu, S., Xu, X., Wang, X., Chang, Q., Wu, J., Li, B., 2022. Quantifying
 latitudinal variation in land surface phenology of Spartina alterniflora saltmarshes across
 coastal wetlands in China by Landsat 7/8 and Sentinel-2 images. Remote Sens. Environ. 269,
 https://doi.org/10.1016/j.rse.2021.112810

- Zhu, Z., Wang, S., Woodcock, C.E., 2015. Improvement and expansion of the Fmask algorithm: cloud, cloud shadow, and snow detection for Landsats 4–7, 8, and Sentinel 2 images. Remote Sens. Environ. 159, 269–277. https://doi.org/10.1016/j.rse.2014.12.014
- Zoffoli, M.L., Gernez, P., Rosa, P., Le Bris, A., Brando, V.E., Barillé, A.L., Harin, N., Peters, S., Poser, K., Spaias, L., Peralta, G., Barillé, L., 2020. Sentinel-2 remote sensing of Zostera noltei-dominated intertidal seagrass meadows. Remote Sens. Environ. 251, 112020. https://doi.org/10.1016/j.rse.2020.112020

List of Figure Captions

- Fig. 1. Map showing the study region (A) which is located on the U.S. mid-Atlantic coast (B). The study region represents the mid-Atlantic sea-level rise hotspot and it encompasses the ecologically and culturally important Blackwater National Wildlife Refuge outlined in yellow. The yellow dots indicate our ground-truth sites in the study region. In addition to ground-truth data, the reference sites for our land cover classification also include sites selected from contemporary drone images
- and high-resolution aerial photos.

995

988

- 996 **Fig. 2.** Accelerated sea-level rise and warming climate in the study region. The data plotted here refers to the long-term temperature and tidal observations at the nearest NOAA meteorological station in Dover, Delaware and the nearest NOAA Tides and Currents station in Cambridge,
- 999 Maryland.

1000

Fig. 3. Coastal landscape reorganization with rising sea-level. (A) Broad-scale vegetation distribution along the land-sea margin, highlighting a "ghost forest" transition zone with dead and stressed trees. (B) Landward upland forest with a closed canopy and lack of understory vegetation. (C) Transition forest undergoing active seawater intrusion, where forest die-off leads to increased light availability for shrub growth and marsh transgression. (D) Established marshland with

occasional remnant standing-dead trees, signifying the completion of marsh transgression.

10061007

Fig. 4. Annual phenological patterns of marsh (A), transition forest (B), and upland forest (C) estimated with Landsat-based NDVI time-series. Plots show data for the most recent five years, and all results are presented as mean ± SD.

1011

Fig. 5. Temporal-trend of peak growing-season NDVI for different coastal vegetation types, estimated using 36 years of data (1984-2020) – the long time-span test (A), 24 years of data (1996-2020) – the intermediate time-span test (B), and 12 years of data (2008-2020) – the short time-span test (C). The linear regression trend line is bounded by the 95% confidence interval. Dotted

lines refer to marginally significant trends $(0.05 \le P < 0.1)$ whereas solid lines represent significant trends at the level of P < 0.05.

Fig. 6. Flowchart for spatially-explicit assessment of forest retreat rate. See text for acronym definition and detailed description of the step by step procedure.

Fig. 7. Accuracy assessment shown as *User's* accuracy (A), *Producer's* accuracy (B), and Overall and Kappa coefficient (C) for the land cover maps generated by the S₂ algorithm at three time-steps (1985, 2000 and 2020).

Fig. 8. Multi-period land cover maps in the study region. The inserted pie charts show the areal percentage of each land cover in the region, and the black boxes (1) and (2) refer to the two zoom-in sites presented in detail by the second (Site 1) and third row (Site 2).

Fig. 9. Comparison of different land cover products in Site 1. The maps presented in the first row were derived from high-resolution (~1 m) aerial photos, serving as the reference for comparison.

The marsh-forest boundary (yellow lines) was manually delineated on the aerial photos, and the differenced maps show the areal changes of coastal forest from Time1 to Time2. Our own maps generated in 2000 and 2020 were plotted in the second row. The corresponding C-CAP and NLCD products were shown in the third and fourth rows, overlaid with black lines indicating areas of transition forest identified by our products.

Fig. 10. Comparison of different land cover products in Site 2. The maps presented in the first row were derived from high-resolution (~1 m) aerial photos, serving as the reference for comparison. The marsh-forest boundary (yellow lines) was manually delineated on the aerial photos, and the differenced maps show the areal changes of coastal forest from Time1 to Time2. Our own maps in 2000 and 2020 were plotted in the second row. The corresponding C-CAP and NLCD products were shown in the third and fourth rows, overlaid with black lines indicating areas of transition forest identified by our products.

Fig. 11. Vertical range shifts of different coastal vegetation over time. Panels on the left represent the distribution histogram of each vegetation type with elevation, and the vegetation-specific mean elevation is indicated by the dotted lines. The right panel shows the vertical migration rate estimated for each vegetation type between 1985 and 2000, and between 2000 and 2020. Coastal forest is the aggregate of transition forest and upland forest.

Fig. 12. Estimated horizontal forest retreat rates between 1985 and 2020 (A), between 1985 and 2000 (B), and between 2000 and 2020 (C) across our study region. Please refer to the text for a

detailed description of the methodology (2.8 Spatially explicit quantification of forest retreat rate).